

INFORMATION TO USERS

This manuscript has been reproduced from the microfilm master. UMI films the text directly from the original or copy submitted. Thus, some thesis and dissertation copies are in typewriter face, while others may be from any type of computer printer.

The quality of this reproduction is dependent upon the quality of the copy submitted. Broken or indistinct print, colored or poor quality illustrations and photographs, print bleedthrough, substandard margins, and improper alignment can adversely affect reproduction.

In the unlikely event that the author did not send UMI a complete manuscript and there are missing pages, these will be noted. Also, if unauthorized copyright material had to be removed, a note will indicate the deletion.

Oversize materials (e.g., maps, drawings, charts) are reproduced by sectioning the original, beginning at the upper left-hand corner and continuing from left to right in equal sections with small overlaps. Each original is also photographed in one exposure and is included in reduced form at the back of the book.

Photographs included in the original manuscript have been reproduced xerographically in this copy. Higher quality 6" x 9" black and white photographic prints are available for any photographs or illustrations appearing in this copy for an additional charge. Contact UMI directly to order.

UMI

A Bell & Howell Information Company
300 North Zeeb Road, Ann Arbor MI 48106-1346 USA
313/761-4700 800/521-0600



Feasibility studies for Laser Spectroscopy of Thorium Ions in a Paul Trap

by

Hongmei Cheng

A thesis submitted to the Faculty of Graduate Studies and Research

In partial fulfillment of the requirements for the degree of

Master in Physics

Foster Radiation Laboratory,
Physics Department,
McGill University
Montréal, Canada
April, 1997

©Hongmei Cheng, 1997



**National Library
of Canada**

**Acquisitions and
Bibliographic Services**

**395 Wellington Street
Ottawa ON K1A 0N4
Canada**

**Bibliothèque nationale
du Canada**

**Acquisitions et
services bibliographiques**

**395, rue Wellington
Ottawa ON K1A 0N4
Canada**

Your file Votre référence

Our file Notre référence

The author has granted a non-exclusive licence allowing the National Library of Canada to reproduce, loan, distribute or sell copies of this thesis in microform, paper or electronic formats.

The author retains ownership of the copyright in this thesis. Neither the thesis nor substantial extracts from it may be printed or otherwise reproduced without the author's permission.

L'auteur a accordé une licence non exclusive permettant à la Bibliothèque nationale du Canada de reproduire, prêter, distribuer ou vendre des copies de cette thèse sous la forme de microfiche/film, de reproduction sur papier ou sur format électronique.

L'auteur conserve la propriété du droit d'auteur qui protège cette thèse. Ni la thèse ni des extraits substantiels de celle-ci ne doivent être imprimés ou autrement reproduits sans son autorisation.

0-612-29674-1

Abstract

This thesis evaluates the suitability of Thorium(*Th*) ions for optical spectroscopic measurements in a Paul trap. A ^{232}Th sample, placed near the ring electrode, is evaporated with a Nd:YAG laser pulse and then selectively ionized by a synchronized dye laser pulse. Ions created inside the trap follow stable orbits and are cooled by hydrogen buffer gas.

The stability and trapping efficiency for the ions are examined at various trap operating conditions. The motion of the ions in the trap is studied with particular attention to volume occupied by the ions in the phase space. With the trap operating at optimum conditions for stability and spectral resolution, laser-induced fluorescence measurements at selected rf phase angles are applied to five optical transitions of Th ions. Results indicate that two transitions are most suitable for spectroscopic studies and 60-80 ions are required to produce a spectrum with signal-to-background ratio of 1:1.

Résumé

Cette thèse évalue la possibilité d'étudier le thorium (Th) par spectroscopie optique à l'intérieure d'un piège Paul. Un échantillon de ^{232}Th , placé près de l'électrode annulaire, est évaporé avec une impulsion laser Nd:YAG et sélectivement ionisé par une impulsion synchrone de laser à colorant. Les ions créés à l'intérieure de la trappe suivent des orbites stables et sont refroidies par un gaz tampon d'hydrogène.

La stabilité et l'efficacité de collection des ions sont examinées sous plusieurs conditions d'opérations. Le mouvement des ions dans la trappe est étudié en portant une attention particulière au volume d'espace de phase qu'ils occupent. Aux conditions optimales de stabilités et de résolution spectroscopique, des mesures de fluorescence induite par laser sont effectuées à certains angles de phase rf sur cinq transitions optiques différentes des ions de Th. Les résultats indiquent que deux des transitions sont adéquates pour l'étude par spectroscopie et que 60-80 ions sont requis pour produire un spectre ayant un rapport signal:bruit-de-fond de 1:1.

To my parents

Contents

1	Introduction	1
2	Experimental Setup	5
2.1	Layout of the experimental apparatus	5
2.2	RFQ or Paul Trap	7
2.3	Ion Extraction and Detection System	10
2.4	Optical Detection	11
2.5	Ultra-High Vacuum System	14
2.6	Laser System	16
2.7	Data Acquisition and Electronics	18
2.8	Overall Experimental Procedure	20
3	Stability Study of the Present Ion Trap System	22
3.1	RFQ trap operation principle and its stability diagrams	22
3.2	Pseudopotential Well of the Trap	27
3.3	Experimental procedure of trapping stability and efficiency tests . . .	28
3.4	Ions trapped as a function of RF voltage at fixed frequency	29
3.5	Trapping efficiency vs f_{RF} with constant q_z	32
3.6	The storage time of trapped ions and chemical reaction inside trap . .	33
3.7	Conclusion	36

4	Trapped Ion Motion and Phase Space Dynamics	37
4.1	Particle Dynamics and Ion trajectories as a function of time	38
4.2	Phase space and phase trajectories for trapped ions	42
4.3	Variation of phase space ellipses with different rf phase angle and trap operating parameters	44
4.4	$\Delta\nu$ Versus RF Phase Angle Measurement	47
4.5	$\Delta\nu$ Versus RF phase angle at different β_r value	51
4.6	Ion Temperature	51
4.7	Conclusion	53
5	Optimizing Detection of LIF from Th Ions	54
5.1	Thorium: Nuclear Properties and Previous Isotope Research Review .	55
5.2	Th Ion Production Process	57
5.3	Laser Spectroscopy Measurements	59
	5.3.1 LIF Detection Procedure	59
	5.3.2 Experimental Results	62
	5.3.3 Discussion	64
6	Summary and Conclusion	67

List of Figures

2.1	Experimental Setup	6
2.2	Schematic diagram of the RFQ trap	8
2.3	The RFQ trap driving circuit diagram	9
2.4	A typical TOF spectrum of ejected Thorium ions	11
2.5	Fluorescence photon collection system inside the trap	12
2.6	The response characteristics of two different photomultipliers	13
2.7	cw tunable dye laser with an intra-cavity frequency doubler	17
2.8	Schematic diagram for data acquisition system	19
2.9	Coincidence gating	20
3.1	A Mathieu stability diagram for the RFQ ion trap	24
3.2	The expanded view of the Mathieu stability diagram employed in ac- tual trapping in three dimensions	26
3.3	Ion number vs RF voltage at $f=150$ kHz	30
3.4	Ion number vs operating frequency at $q_z=0.40$	33
3.5	TOF measurement show the Th and Th oxide conversion	35
4.1	Trapped ion trajectories	41
4.2	Ion trajectories in phase space-I	43
4.3	Ion trajectories in phase space-II	45
4.4	The Th spectrum pumped at 322.8 nm	48

4.5	A group of laser spectra at different RF phase angles measured by phase-selective LIF	49
4.6	Spectral full width(FWHM) vs RF phase angles. The data correspond to operating condition ($a_z=0$, $q_z=0.495$)	50
5.1	The RIS scheme of Th	58

List of Tables

3.1	Results Table	31
3.2	D_z values for low cutoff points	32
5.1	Thorium Lines Detected and Detection Results	61

Acknowledgments

Foremost, I would like to thank my supervisor, Professor Jonathan Lee for all his guidance in both the research and writing of this thesis. His participation in running experiments, searching for solutions and discussing data at all stages of the process were vitally important. Without his detailed input, encouragement and patience, I would not have finished my master's studies.

My deep thanks also goes to Research Associate, Dr. Sidney Gulick. He helped me in every aspect of the research, spending hours of his time collaborating with me on experiments, problem-solving, and proof-reading my thesis. Without his enormous help in all of these aspects, I would have accomplished nothing.

As well, I would like to thank Professors John Crawford and Fritz Buchinger. Several times they came to my rescue as I struggled to tune the CW laser. I also thank them for their overall encouragement throughout my writing process.

In addition to those mentioned above, I would like to thank Professor Jean Barrette for his continual encouragement throughout my studies here at McGill; to Steve Kecani and Leo Nikkinen for their technical support; to Dirk Richter, who helped me with detailed experimental work; to Taeman Kim for his drawing software expertise, to Pedro Martinez, for help with my data table; and to Roger Lacasse, for his French translation of my abstract and help in Latex.

All in all, I want to thank all the people who played a role, either in my actual studies or in adjusting to Montreal life, during my master's studies.

Finally, a special thanks to my parents for all their love and support.

Chapter 1

Introduction

Atomic spectroscopy has played an important role in nuclear physics since its beginnings. Because the nucleus is an inseparable part of an atomic system, much information about nuclei can be obtained by studying the atomic system. Through high-resolution atomic spectroscopy, valuable and important nuclear structure parameters can be measured indirectly.

During the past twenty years, one of the active areas of research in nuclear physics has been the measurement of hyperfine structure(hfs) and isotope shifts(IS) over a long chain of isotopes for certain elements. Hyperfine structure gives us information on nuclear spins, the nuclear magnetic dipole and electric quadrupole moments. Isotope shifts are very useful for measuring the change in charge radii of nuclear ground states.

With the introduction of laser techniques in the early 1960's, unstable nuclides have become much more accessible for study. Especially after tunable dye lasers of high monochromaticity and high intensity were developed in the early 1970's, measurements of nuclear structure parameters have been greatly advanced through application of high precision laser spectroscopy.

Presently, about 500 isotopes of more than 30 elements have already been investigated in long isotopic chains by laser methods. Reviews of the developments in laser

spectroscopic studies of hfs and IS of radioactive isotopes can be found in [1] [2] [3] [4]. Systematic variations of nuclear charge radii have been compiled in [5]. In many cases, laser spectroscopy measurements are the only ways that can be used to determine these quantities for short-lived nuclei.

Most of the measurements referred to above were carried out using a collinear laser method at ISOLDE, CERN [6] [7] [8]. In collinear laser spectroscopy, a fast ion beam from ISOLDE interacts with a superposed laser beam, allowing laser spectroscopic studies of isotopes far off stability. This method is sensitive and versatile, and well suited for studying short-lived isotopes.

For the isotopes for which it is difficult to produce an ion beam with sufficient intensity, the collinear laser technique cannot be employed. For some of these isotopes, other laser spectroscopy methods have been developed. Among them, on-line resonance ionization spectroscopy (RIS) has been applied in Saint Petersburg to a large number of radioactive rare-earth isotopes [9]. Another method involves the use of RIS of laser desorbed radioactive samples to study the radioactive "daughter" nuclei from nuclear decay. The sensitivity of this method is comparable to the collinear method and was applied to the studies of radioactive isotopes of the noble metals Au and Pt by several groups [10, 11]. Foster Radiation Lab at McGill participated in this work [10].

Because some isotopes can not be easily produced in isotope separators, a more suitable and sensitive method was developed. This is laser spectroscopy employing a radio-frequency quadrupole ion trap (RFQ trap or Paul trap). The RFQ trap was invented in 1958 by Paul [12]. Using a relatively weak confining electric field, the Paul trap enables us to store charged particles for extended periods within an isolated and limited space. Only a small number of trapped ions is needed for a measurement. Even detection of a single confined ion has been demonstrated [13].

Although laser spectroscopic studies have been performed in traps since early 1977 [14], such measurements on radioactive isotopes were not implemented until

1988. A group from Germany first introduced Th isotopes into a Paul trap by evaporating some samples on a tantalum wire and ionizing them by an electron beam [15, 16, 17]. Ions then were probed by incident laser beams. For the Th ions, sub-Doppler resolution was obtained by using a two step excitation scheme [17]. A drawback of this approach is that electron beam ionization is non-selective and many kinds of contaminant ions can be produced and trapped at the same time due to the poor mass selectivity of the Paul trap. Therefore, in previous work of our lab at McGill University, WenZheng Zhao developed a more selective system employing a Paul trap for laser spectroscopic studies of radioactive elements [18, 19, 20]. This system incorporates a new method for ion production and accumulation inside the trap. A Nd:YAG laser is used to desorb a target material and subsequently the RIS process is employed to selectively ionize atoms of a specific element directly inside the trap. Both ion-ejection time-of-flight detection and laser-induced fluorescence(LIF) measurement have been incorporated in the setup.

With a spectral resolution of 1 GHz, hfs of ^{177}Hf and ^{179}Hf were studied experimentally and the IS of the radioactive ^{172}Hf was also measured in Zhao's work [18]. He was able to detect a ^{172}Hf resonant peak corresponding to only 20 trapped ions. His work demonstrated the usefulness of the Paul trap of our experimental system and encouraged us to pursue further studies of other previously inaccessible radioactive isotopes.

The isotope ^{229}Th is particularly interesting because it has been suggested that the first excited metastable state in ^{229}Th , which should have $J^\pi=3/2^+$, may be found within 3.5 ± 1 eV of the $5/2^+$ ground state [21, 22]. The existence of an excited nuclear state at such a low energy, especially one that is connected to the ground state via an M1 transition, presents an opportunity to investigate a variety of interesting phenomena related to the interaction of the nucleus with its electronic environment.

Although the predicted low energy metastable state of ^{229}Th has provoked extensive studies in recent years [23, 24, 25], so far there is no direct experimental evidence

for the existence of this metastable level. With an excitation energy below that of the most loosely bound atomic electron in thorium, and its unknown lifetime, the decay of the excited state may not be able to proceed via an internal conversion process. If the ^{229}Th ions produced from ^{233}U alpha decay can be caught in a trap, it is conceivable that we can measure and identify the hyperfine structure of the low energy isomer($J^\pi=3/2^+$) by comparing it with the known hyperfine structure of the ground state($J^\pi=5/2^+$). Furthermore, as outlined by some Russian researchers [25], it could be possible to induce nuclear excitation from a resonant electronic state excited by a laser. The low energy level isomers could be populated first and the delayed photons from de-excitation of the M-state could then be observed. Since production of the isotope ^{229}Th is difficult, and the lifetime of the low energy isomer is unknown, to prepare for such an proposed experiment, a high sensitivity experiment and detection system and high resolution laser spectroscopy are needed.

This work represents a feasibility study for this experiment and is based on Wenzheng's Hf work in this lab. We did a series of experiments using a ^{232}Th source, covering three areas: A study of the stability of the trapped ions under various operating conditions and the efficiency of production and trapping; evaluation of the effects of various trap operating parameters on spectral resolution; and the evaluation of sensitivity, resolution of different optical excitations and detection schemes.

In this thesis, the experimental setup will be described in Chapter 2. Experimental results and discussions make up Chapters 3,4,5 and a summary and conclusion form Chapter 6.

Chapter 2

Experimental Setup

In this chapter, the experimental setup is described. First, a general layout of the experimental system is given, then the detailed descriptions of each individual component are presented.

2.1 Layout of the experimental apparatus

The general setup of our experiments is shown in Figure 2.1.

The RFQ trap(Paul trap) is placed inside an ultra-high vacuum(below $10^{-8} Pa$) chamber. It is made up of three electrodes in which various holes are drilled for the passage of laser beams, ion extraction and photon detection. A sample material is put into a target holder which is positioned near the bottom hole of a central ring electrode. Laser pulses from a Nd:YAG laser pass through the top hole and vaporize the sample materials into the trap center. Synchronized RIS dye laser pulses pass through a horizontal hole on the ring electrode and hit the vapor cloud in order to selectively ionize a chosen element. Some d.c. and RF voltages are applied to these electrodes, and with the resulting electric field inside the trap, certain kinds of ions will follow various stable trajectories and remain inside the trap for a long time.

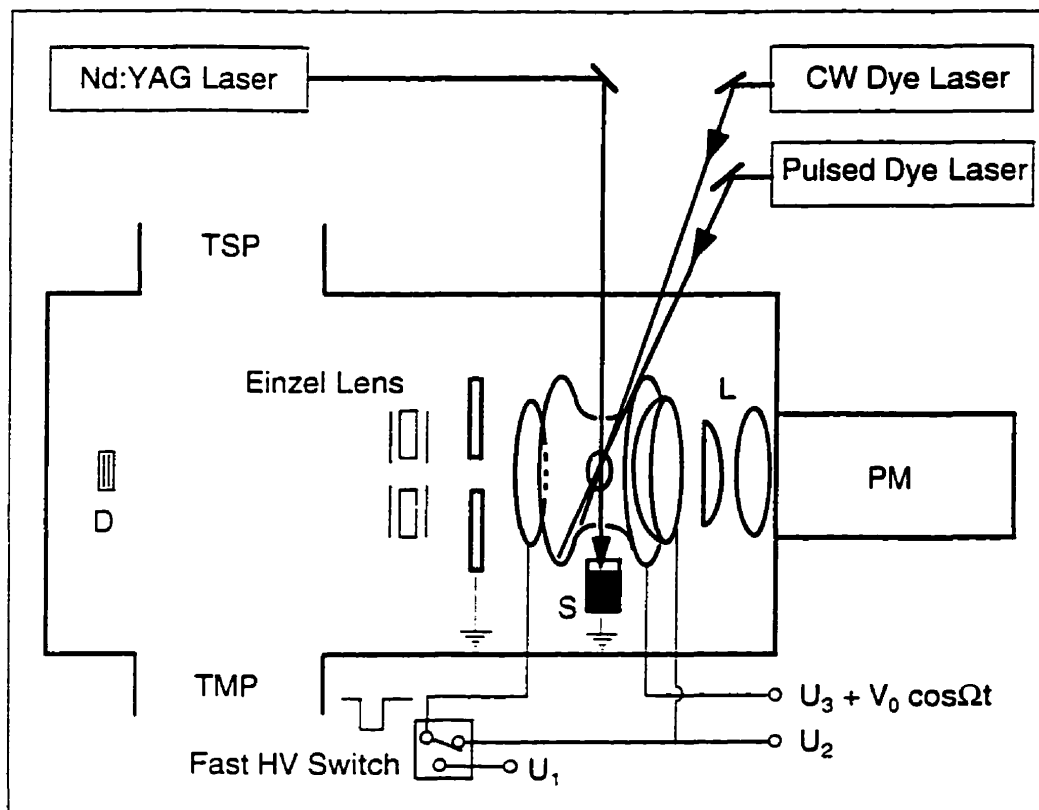


Figure 2.1: Experimental Setup: S:Target with sample; PM: Photomultiplier; D: Micro-channel Plate Detector; TSP: Titanium Sublimation Pump; TMP: Turbo-molecular Pump; L: Optical lenses. The RIS and cw laser beams are perpendicular to the YAG beam and pass through the horizontal pair of holes

On one side of the ion trap (shown on the left side of the trap in Figure 2.1), the ion extraction and detection system is attached. Trapped ions can be extracted by applying a negative pulse to the extraction electrode. The ions are then focused by an Einzel lens, and hit the Micro-Channel Plate (MCP) detector (D in figure 2.1). The signal from the MCP detector can be displayed on a scope to reveal a time-of-flight (TOF) spectrum of the ions stored in the trap. This gives us information about the mass distribution and the number of the trapped ions.

On the other side of the trap there are optical lenses and filters as well as a photomultiplier (PM on Figure 2.1) for fluorescence detection. A cw dye laser beam passing through the horizontal holes in the ring electrode can be used to probe the trapped ions. By scanning the cw dye laser wavelength across a resonance transition, the laser-induced fluorescence (LIF) spectrum of the trapped ions can be obtained.

The trap is assembled inside an ultra-high vacuum chamber. This chamber is made of stainless steel and is bakeable to 400°C . A computerized digital data acquisition system stores fluorescence data and permits us to see the LIF spectrum on the computer screen. With the stored data, we can do further measurement, analysis and calculation of the nuclear properties we are interested in, such as hyperfine structures and isotope shifts.

In the following sections, each individual part of the setup will be described in detail.

2.2 RFQ or Paul Trap

Figure 2.2 shows the configuration of the RFQ trap used in the setup. It is made of stainless steel and consists of three electrodes of hyperbolic shape: a ring electrode with a central radius r_0 of 20.3 mm and two endcap electrodes with an endcap separation spacing of $28.7\text{ mm}(\sqrt{2}r_0)$.

The extraction endcap on which an extraction pulse is applied has a hole with a

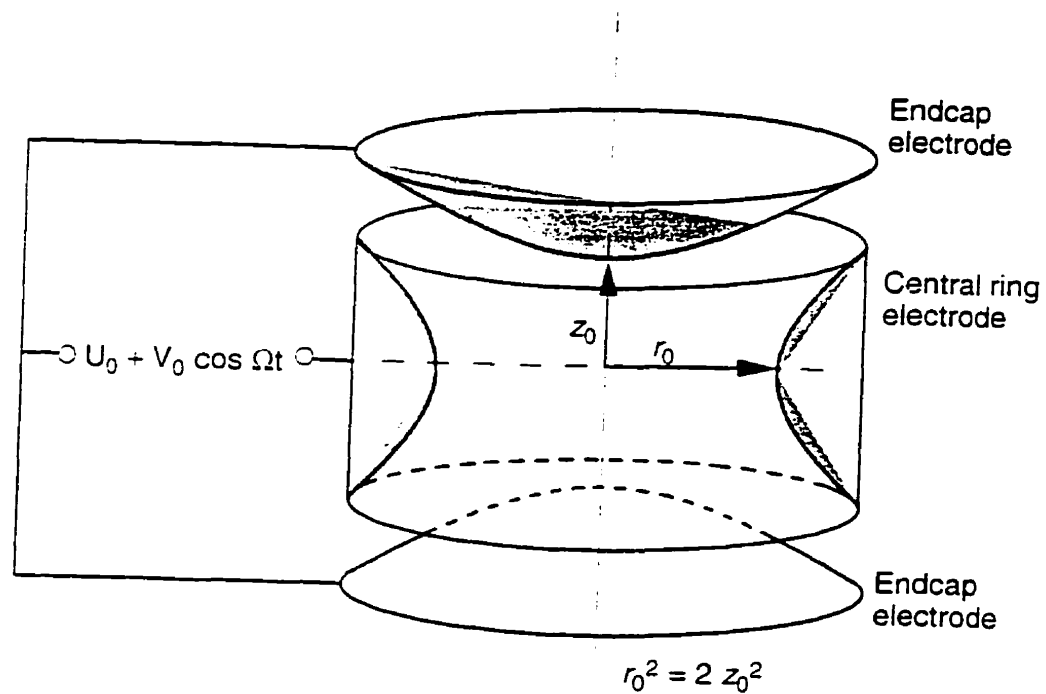


Figure 2.2: Schematic diagram of the RFQ trap

diameter of 10 mm. For the fluorescence photon collection, a 26 mm hole is drilled in the other endcap. These holes are covered with a conducting mesh to preserve the hyperbolic shape of the electrodes. Four holes of 6.4 mm diameter are located symmetrically around the central axis on the side of the ring electrode. They allow laser beams from different directions to pass through the center.

Target material on a graphite substrate is put into the recessed end of a stainless steel machine screw and the screw is positioned near the inner edge of the bottom hole on the ring electrode.

To operate the RFQ trap, an appropriate radio-frequency voltage V_0 with angular frequency Ω combined with a dc bias U_0 is applied to the ring electrode as shown (U_0

is the bias voltage between the ring and the endcaps, and $U_0=U_3-U_2$). The effective voltage at the center of the trap (the kinetic energy of the extracted ions) is $(U_2+U_3)/2$. Figure 2.3 is a schematic diagram for all the voltage supplied to the trap.

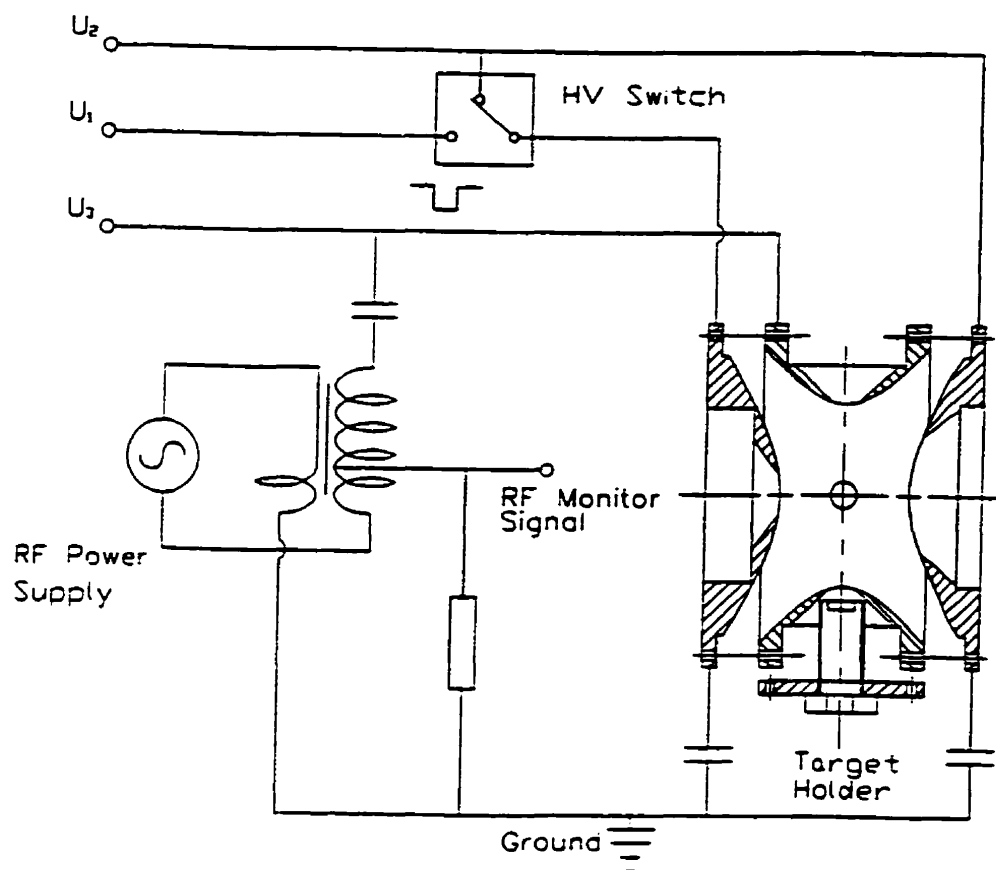


Figure 2.3: The RFQ trap driving circuit diagram

In our system, the dc bias U_0 can be adjusted from 0 to 40 V. The target holder is biased to the same voltage as U_3 (usually 800V). The extraction voltage U_1 applied

to the extraction electrode will be described later in section 2.3.

2.3 Ion Extraction and Detection System

After the ions are trapped, they are expected to move with stable trajectories and remain inside the trap unless their trajectories are perturbed by collisions. We want to detect them by extracting the ions out to a micro-channel plate detector and figure out the mass distribution and ion numbers inside the trap. For these purposes, the ion extraction system and time of flight set-up are used.

When a negative pulse is applied to the extraction endcap, the ions inside the trap are accelerated towards the extraction endcap. Passing through the mesh hole in the endcap, the ions are accelerated by the electric field towards the Einzel Lens. After being focused by the Einzel Lens, the ions finally drift to the micro-channel plate detector, which is made of two micro-channel plates mounted in parallel. A high voltage (around 1.5 kV) is applied to the micro-channel plate detector. Half of this voltage is across each micro-channel plate. The typical gain of the 2-plate detector is about 10^6 . Ions of different masses reach the micro-channel plate detector at different times. The signal from the micro-channel detector goes through a preamplifier before entering a digital storage scope to form a time-of-flight (TOF) spectrum.

By knowing the distance between the trap center and the detector (40cm), the magnitudes and positions of the peaks in the TOF spectrum yield information on the mass distribution of the ions in the trap. The area under each peak can give the number of ions of each mass trapped inside the trap. Figure 2-4 shows a typical TOF spectrum obtained from ejected Thorium ions. The ions were extracted after remaining inside the trap about 30 seconds. From the mass distribution in time we deduce that the two peaks correspond to Th^+ and ThO^+ ions respectively. The typical spectrum resolution ($M/\Delta M$) is about 60. This resolution is limited by our short time-of-flight drift chamber.

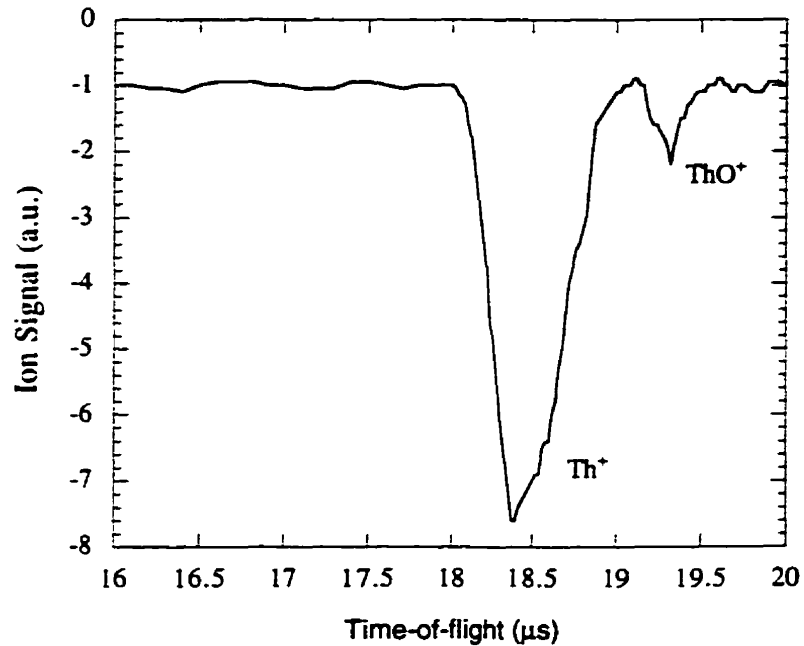


Figure 2.4: A typical TOF spectrum of ejected Thorium ions

A time delay unit is used to control how long to accumulate and store the ions and when to extract them. To extract the trapped ions, the delay unit initiates an ejection pulse, which triggers a high voltage switch and produces a negative pulse on the extraction endcap. For the best time-of-flight spectrum, the ejection timing is carefully optimized relative to the RF phase because the interaction between the extraction and RF fields inside the trap affects the time-of-flight spectrum [26].

2.4 Optical Detection

After the ions are trapped, the stored ions can be optically excited by a probing laser. The resonances are detected by monitoring the spontaneous emission following the absorption. Two silica lenses make up the photon collection system inside the vacuum chamber. One is a planoconvex lens of 40 mm in diameter with a focus of

$f=50$ mm. The other is a symmetry-convex lens of 50 mm in diameter with $f=75$ mm. The optical components are shown in Figure 2-5. The first lens was put as close as possible to the trap center in order to get a large solid angle (6%) for efficient collection. The light collected by the lens system is focused on the photocathode of a photomultiplier. The photomultiplier is placed outside of the vacuum chamber, on the other side of the sapphire chamber window, about 200 mm away from the trap center.

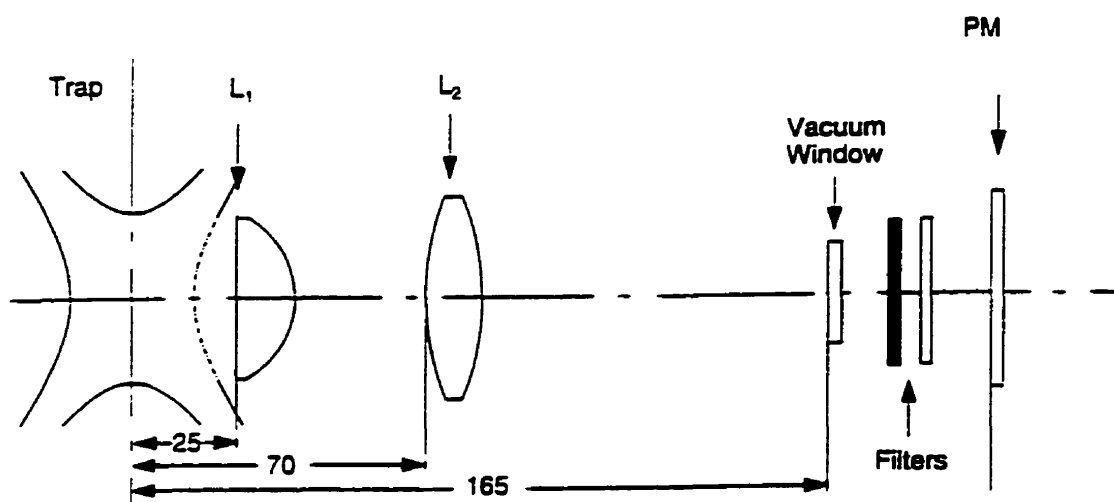


Figure 2.5: Fluorescence photon collection system inside the trap

Two different kinds of photo-multipliers are used to detect the fluorescent light in the experiments. One is an RCA 8850 and the other is an RCA C31304. For the laser induced fluorescent detection, the signal to background ratio is an important concern, so efforts were made to suppress the background count and increase the photon counting signal.

The RCA 8850 photomultiplier was used to observe excitation schemes producing

fluorescence in the range of 250-600 nm. The RCA 31034 has a much greater sensitivity in the near infrared and longer visible range but has the disadvantage that it must be cooled to reduce the dark current. Figure 2-6 compares the two photomultiplier photocathode spectral response characteristics.

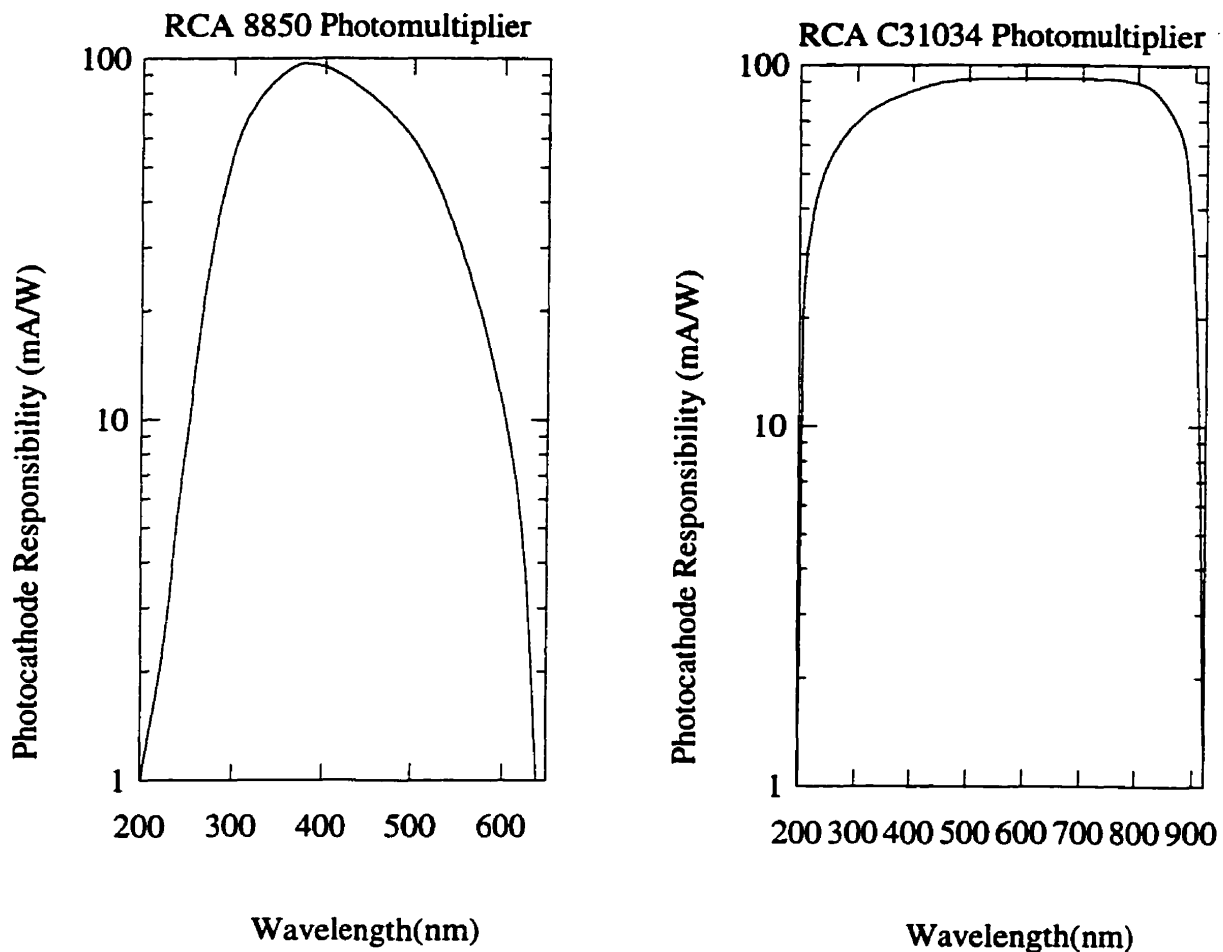


Figure 2.6: The response characteristics of two different photomultipliers

The photocathode of the RCA 8850 photomultiplier is 45 mm in diameter. Typically, a voltage of about 1600V is applied between the anode and the photocathode. The dark current counting rate under these conditions is about 180 cps.

The RCA 31034 is an 11-stage photomultiplier. It has a small GaAs:Cs-O photocathode (10mmx4mm), ultraviolet-transmitting glass windows, and an in-line copper

beryllium dynode structure. This photomultiplier is designed for use at low temperatures (-20°C). Cooling reduces the dark current to an acceptable value in order to fully exploit the performance capabilities of the tube. The cooling of the photomultiplier tube is accomplished by Peltier elements and water circulation.

In addition to the collection lenses assembled inside the trap, two elements were added inside the RCA 31034 photomultiplier cavity. One is an aspheric glass condenser lens of 50 mm in diameter with a focus length of 20 mm. The other is a flat glass window. This alignment helps to further focus the light to hit the small photocathode window.

Because the RCA C31034 photomultiplier is so sensitive, many efforts were made to reduce the background counts. Several filters and a hot mirror were combined in different ways to sufficiently suppress the scattered light from the laser and other sources so only the fluorescence is detected by the photomultiplier.

2.5 Ultra-High Vacuum System

The ultra-high vacuum system includes the vacuum chamber and two pumps.

The vacuum chamber has two six-sided 8" vacuum crosses sealed with Con-flat flanges. The whole chamber is pumped by a turbo-molecular pump (Balzers TPU180H) with a pumping speed of 180 L/s. A mechanical pump (Balzers DUO1.5A) serves as a backing pump. The ultimate pressure of the system can reach 10^{-8} Pa.

In order to improve the vacuum to provide adequate storage times for the trapped ions, we employed two heat sources to desorb surface contaminants from the trap and the reservoir of the chamber. Inside the chamber, there are 4 300-Watt halogen lamps installed for baking. Sometimes these lamps are also used to illuminate the inner chamber for alignment purposes. Outside the chamber, five 500-Watt heating tapes are wound around the vacuum chamber and covered with aluminum foil to reduce radiation losses.

A mini-titanium ball from Varian installed inside on one side of the vacuum chamber is often used to effectively purify the residual reactive gases. When the titanium ball is heated at a high current of 45A, the titanium atoms of the heated ball sublimate out and form a fresh Ti coating on the inner wall of the chamber [27]. This coating reacts with the impurity molecules which collide with the wall and make stable compounds which stick to the wall. This type of pumping is partially effective in clearing contaminants which react with active trapped ions. The titanium ball is also used as an inside heating source by operating it at a comparatively low current (30A) in order to avoid too much sublimation of titanium. The heating elements are controlled by variacs.

A needle valve allows us to regulate the pressure of a buffer gas (research grade hydrogen with purity 99.9995%) inside the chamber when necessary. The buffer gas has two main purposes: collisional cooling of the trapped ions and optical quenching of ion metastable states to ground states.

To start baking, low voltage is applied to heat the tapes and halogen lamps and to let the system warm up gradually for a while. Then the voltages are increased to reach a temperature of $200^{\circ}C$ to bake overnight. Usually, when the system is baked at the full temperature, hydrogen buffer gas is leaked into the chamber with a pressure of 10^{-3} Pa because it has been found to accelerate the out-gassing of the system [18]. After overnight baking and cooling for more than 30 hours, the whole vacuum chamber can reach the pressure 10^{-8} Pa. At this time, the titanium ball is used again at high current(45A) for 30-60 minutes to form a fresh titanium coating on the inner wall of the chamber. The coating remains effective for a long time because the chamber base pressure is very low.

2.6 Laser System

Five different kinds of lasers have been used in the experimental setup including a Nd:YAG laser, an excimer laser, a pulsed dye laser, an Ar^+ laser and a cw ring dye laser. A Nd:YAG laser is used as a desorption laser to evaporate atoms from the sample source. Then a pulsed dye laser pumped by an excimer laser is used to resonantly ionize the atoms. While the ions are in the RFQ trap, the probing beam from a cw ring dye laser pumped by an Ar^+ laser excites the confined ions. Then the emitted fluorescence of various transitions can be detected.

The Nd:YAG laser used for vaporizing the sample is JK Lasers System 2000. It has a output wavelength of 1064 nm. This laser produces a pulse of about 10 ns width. The pulsed beam goes through a polarizer and several prisms to a lens to be focused on the target surface. The adjustable polarizer is used to attenuate the YAG laser pulse output energy. The lens is mounted above the vacuum chamber sapphire window to focus the laser beam onto the sample in order to produce a high efficiency desorption. A video camera is mounted along the optical axis above the focus lens in order to monitor the position and area of the laser spot on the target substrate.

The pulsed dye laser (Lambda FL2002) is pumped by a XeCl excimer laser (Lambda EMG 201MSC). The pulse energy of the pump laser reached up to 260 mJ at a wavelength of 308 nm. The pulsed dye laser can be tuned through a wavelength range of 332-970 nm by using different dyes. By employing a frequency-doubling crystal (SHG), the tuning range can be extended into the ultraviolet(UV). The dye used in our experiments is Coumarin 540A, which has a range of 513-612nm.

For the pulsed dye laser, the measured conversion efficiency is about 3-5%. After the doubling crystal, the laser radiation light obtained is up to 10-20 mJ/pulse. The estimated ionization efficiency is about 15%. The pulsed laser beam (green and UV) is reflected by two prisms through the chamber sapphire window, hits the cloud of atoms and exits through the opposite window.

A master trigger signal goes to the Nd:YAG flash lamp with a repetition rate adjustable from 0.5Hz to 10Hz. There is an 8-20 μs delay between the Nd:YAG Q-switch pulse and pulsed dye laser trigger signal to allow the vaporized atoms produced by the YAG laser time to reach the trap center for resonant ionization. This delay is controlled by the master trigger generator. The master trigger generator also can synchronize the output triggers to the trap RF phase. This permits the study of the relationship between phase and trapping and extraction efficiency described in Chapter 4. Two delayed synchronized outputs are sent to trigger the Nd:YAG Q-switch and the excimer laser.

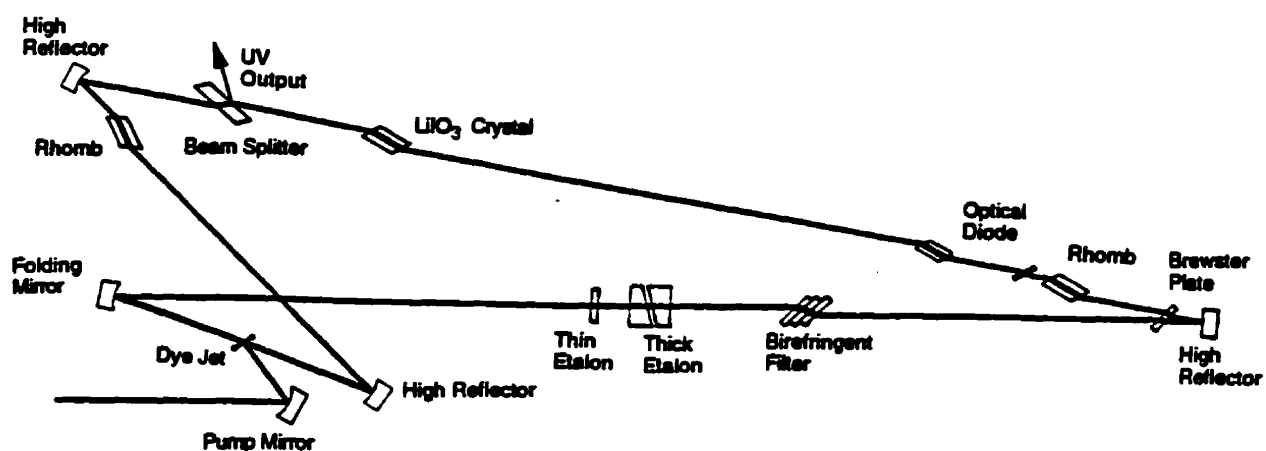


Figure 2.7: cw tunable dye laser with an intra-cavity frequency doubler

For the excitation of *Th* ions for transitions in the UV and visible region, two different cw ring dye lasers are used. They are pumped by a Coherent Innova CR-12 Ar^+ laser with an output all-line power of 8-11W. For the lines in the UV range, the Coherent CR-699-21 ring dye laser (Figure 2.7) which contains an intra-cavity frequency doubler is used. The second harmonic generation is efficient because of

the high fundamental laser power density inside the ring dye laser cavity. In the experiments, to keep the LiIO₃-SHG-crystal dry (the crystal is hygroscopic), a dry nitrogen gas stream surrounds the unit permanently. For that purpose, a heater was built to boil liquid nitrogen to produce a flow of N₂ gas. The UV beam produced by the crystal is separated by prisms from the fundamental laser beam inside the laser cavity. Usually, the output power of the fundamental laser light is about 1.5-2.5 mW, and the UV output is about 1 mW. For our work, DCM dye is used to produce the required wavelength laser radiation. Using DCM dye and the LiIO₃ doubling crystal provides a UV tuning range of 318-350 nm.

Another cw ring dye laser without an intra-cavity SHG crystal is used at a wavelength of 584 nm. The dye mixture used is Rhodamine-6G, which is prepared by dissolving one gram of powdered dye in 50 ml reagent methanol and then adding this mixture to about 650 ml of Ethylene Glycol. This R6G dye covers a wavelength range of 560-657 nm, and its peak is at 575 nm. The input pump power for this ring dye laser is about 6W-9W. Normally, up to 400 mW laser radiation output power at wavelength 584 nm can be obtained.

For driving the scanning of the cw laser, A DAC controlled by computer gives a stepped dc voltage (+5V to -5V). Usually, the scan step is set at 125 ms. A series of thumb wheels on the laser electronic control box controls the size of the wavelength scan. In order to calibrate the laser scanning range and check the laser performance, a confocal etalon (150MHz FSR) and a spectrum analyzer (1500MHz FSR) are used.

2.7 Data Acquisition and Electronics

Figure 2.8 shows a schematic diagram of the data acquisition system in the setup.

The de-excitation fluorescence photon signal collected from the photomultiplier (PM) passes a preamplifier and a fast amplifier. Then the signal goes to a discriminator. After the discriminator, the photon count output is sent to a CAMAC counter

described more fully in Chapter 4.

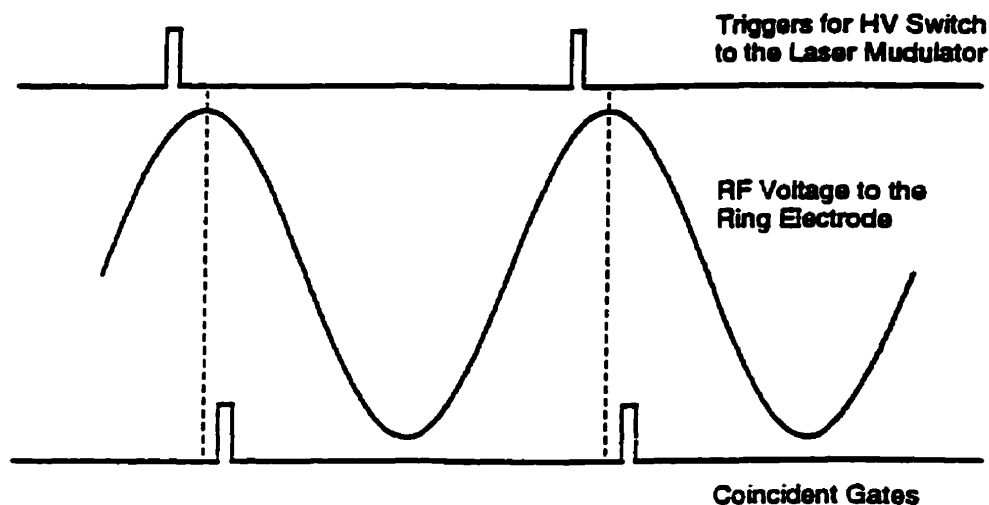


Figure 2.9: Coincidence gating

The data acquisition program used in the experiments sets the cw laser scan rate and the number of scans to be recorded. It stores each individual scan and the sum of a series of scans. The saved traces may be retrieved to be reviewed later. The data are also accessible for further analysis. An ADC module is also connected to the computer to record the interference pattern from the confocal etalon. At each step the ADC output and photon counts are displayed on the screen so the precise spectral resolution can be measured.

2.8 Overall Experimental Procedure

The typical procedure of our experiments starts with putting the sample materials inside the trap chamber. The source on a graphite substrate is put into the recessed end of a machine screw. The screw is positioned near the bottom hole in the ring

electrode of the trap. The vacuum chamber which contains the trap is then sealed and baked for about 30 hours to get a high vacuum system.

To produce ions from the source, first a Nd:YAG laser beam is used to hit the sample material and evaporate neutral atoms from the target substrate. At this stage, we usually look at the position and size of the desorption laser spot on the target through a video camera, and then adjust the beam to achieve a satisfactory desorption result. When the Nd:YAG laser is properly adjusted, a cloud of source atoms is injected into the trap cavity. The RIS pulsed laser beams then interact with the cloud of atoms to resonantly ionize the selected atoms. With proper buffer gas pressure, The ions will condense in the center of the trap and be stored there under the RF field provided by the trap circuit.

To detect the trapped ions, we can either do a time of flight measurement or a LIF measurement. By applying a negative pulse to the extraction endcap, the ions inside the trap can be extracted out to a micro-channel plate detector, producing a time of flight spectrum on a digital storage scope. Through TOF measurements, the mass distribution, the quantity, and the storage time of the trapped ions can be obtained directly.

The ions inside the trap can be stored and detected by a probing laser to complete a LIF measurement. The cw laser light optically excites the ions. The de-excitation fluorescence photon signal is collected by the optical lens inside the trap and is detected by a photomultiplier. Signals from the photomultiplier are amplified, sent to a discriminator and counted with a counter with a phase-locked coincidence gate. Then the signal spectrum measured is shown on the computer screen and stored in the computer memory.

Chapter 3

Stability Study of the Present Ion Trap System

To improve our understanding of the operating parameters of the trap system and to study their effects on the trapping ability, stability and the dynamics of the trapped ions, a systematic study of the effects of varying trap RF frequency and amplitude was carried out.

In this chapter, I will first give a general theoretical background and then present my experimental results.

3.1 RFQ trap operation principle and its stability diagrams

The ion trap involved in our experiments is an RFQ trap or Paul trap. To produce the required three-dimensional rotationally symmetric quadrupole field, the electrode structure illustrated in Figure 2.2 is used.

In the ion trap structure, the two "end-caps" and the ring electrode have cross-sections in the rz plane which are complementary hyperbolas with a ratio of $\sqrt{2}$ in

the semi-axes (r_0/z_0). Usually, the end-caps of the RFQ trap are grounded, and only a single potential Φ_0 needs to be applied to the ring as shown in Figure 2.2. This potential is

$$\Phi_0 = U + V \cos \Omega t \quad (3.1)$$

where U is a direct dc voltage, V is the zero to peak amplitude of the RF voltage and $\Omega(=2\pi f)$ is the angular frequency of the RF voltage. The potential at any position(x,y,z)can be represented as [28]

$$\Phi = \frac{\Phi_0(x^2 + y^2 - 2z^2)}{2r_0^2} + \frac{\Phi_0}{2} \quad (3.2)$$

The equations of motion of an ion in the trap are given by $m\ddot{x}=eE_x$ and so on. These are derived as

$$\ddot{z} - (2e/mr_0^2)(U + V \cos \Omega t)z = 0 \quad (3.3)$$

$$\ddot{r} + (e/mr_0^2)(U + V \cos \Omega t)r = 0 \quad (3.4)$$

If we define trapping parameters as:

$$a_z = -2a_r = \frac{-8eU}{mr_0^2\Omega^2} = \frac{-4eU}{mz_0^2\Omega^2} \quad (3.5)$$

$$q_z = -2q_r = \frac{4eV}{mr_0^2\Omega^2} = \frac{2eV}{mz_0^2\Omega^2} \quad (3.6)$$

$$\xi = \frac{\Omega t}{2} \quad (3.7)$$

we can see, both(3.3) and (3.4) reduce to the general form:

$$\frac{d^2u}{d\xi^2} + (a_u - 2q_u \cos 2\xi)u = 0 \quad (3.8)$$

where u represents either r or z . Equations(3.3) and (3.4) are of the Mathieu type and eqn.(3.8) is the Mathieu equation in its canonical form. Solutions to the Mathieu equation can be expressed by

$$u(\xi) = \alpha e^{\mu\xi} \sum_{n=-\infty}^{\infty} C_{2n} e^{2in\xi} + \alpha' e^{-\mu\xi} \sum_{n=-\infty}^{\infty} C_{2n} e^{-2in\xi} \quad (3.9)$$

where α and α' are integration constants depending on the initial conditions: that is u_0 , \dot{u}_0 and ξ_0 . The constants C_{2n} and μ depend on the values of a and q and not on the initial conditions [28, 29]. There are two types of solutions to (3.9) and they depend on the nature of μ . The stable trajectories of ions come from solutions where $\mu=i\beta$ is pure imaginary and β is not a whole number. Because μ depends only on a and q , the conditions for stability can be represented on an a - q diagram or stability diagram. Figure 3.1 shows a Mathieu stability diagram for the RFQ ion trap.

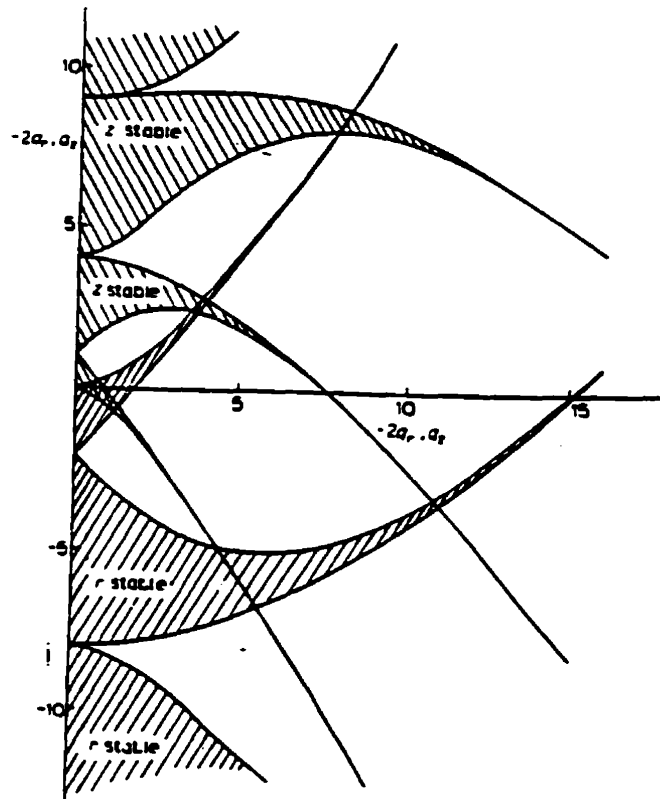


Figure 3.1: A Mathieu stability diagram for the RFQ ion trap

From the above diagram, the stability regions defining the a, q values corresponding to the solutions of the Mathieu equation which are stable in the z direction are labeled z -stable in the figure, and the regions corresponding to solutions which are stable in the r direction are labeled r -stable. Because $a_z = -2a_r$ and $q_z = -2q_r$, the size of the r -stable region is twice the size of z -stable region. The region of simultaneous stability comprises the intersection of these two regions. Ions stay in the ion trap only if they are stable in both r and z directions simultaneously.

The stability diagram in Figure 3.2 is an expanded view of part of Figure 3.1, and is usually employed in actual ion trapping. It is used to analyze the nature of the ion trajectories for any applied voltages U and V by determining β_z and β_r , and considering the motion in the r, z directions independently. The lines are contours of constant β . The stable region is bounded by the limiting values $\beta_{r,z} = 0, 1$ and contains the (a, q) area in which μ is purely imaginary.

Actually, this stability diagram can be considered as the outline for stable ion trap operation. For fixed values of r_0, ω, U and V , all ions of the same m/e have the same a and q values and the same (a, q) point in the diagram. If the operating point (a, q) is within the stable region ($0 < \beta_{r,z} < 1$), the ions will then follow a stable orbit. There is thus a wide range of (a, q) conditions where ions formed within the quadrupole ion trap might be expected to have stable trajectories and remain trapped in the trap indefinitely unless their trajectories are perturbed by collisions.

The complete solution of (3.9) for ion position in the stable region can be expressed as [28]

$$u(\xi) = A \sum_{n=-\infty}^{\infty} C_{2n} \cos(2n + \beta_u)\xi + B \sum_{n=-\infty}^{\infty} C_{2n} \sin(2n + \beta_u)\xi \quad (3.10)$$

The ion trajectory consists of fundamental oscillations (macro-motion) of frequency ω_0 and a number of higher-order components of frequency ω_{hf} .

The fundamental frequency of the macro ion motion is

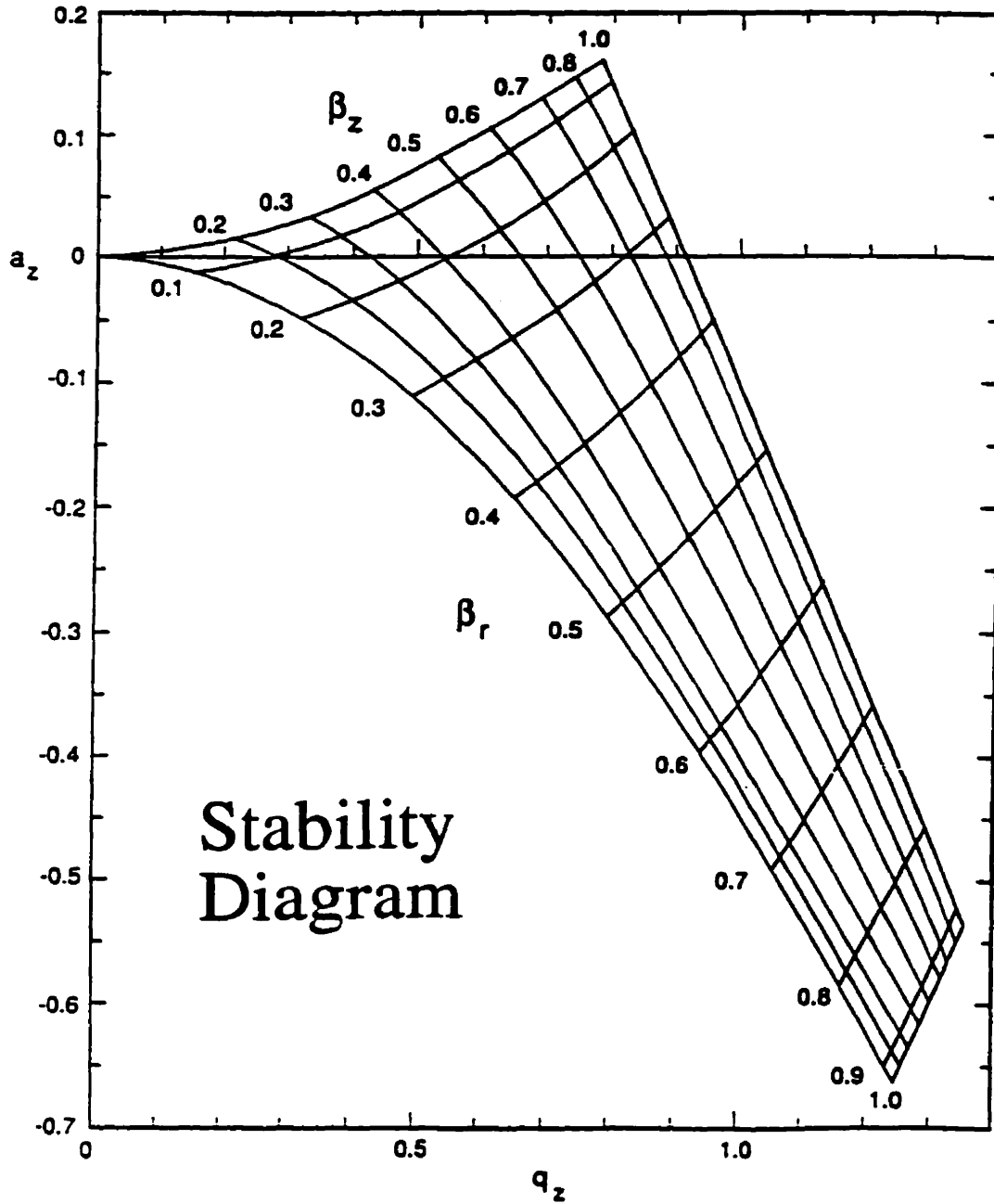


Figure 3.2: The expanded view of the Mathieu stability diagram employed in actual trapping in three dimensions

$$\omega_0 = \frac{\beta_{r,z}\Omega}{2}, (n = 0) \quad (3.11)$$

and the high-frequency oscillating terms are

$$\omega_{hf} = (n + \frac{\beta_u}{2})\Omega, (n = 1, 2, \dots) \quad (3.12)$$

where u stands for either r or z direction. For $\beta \leq 0.4$,

$$\beta_u = (a_u + \frac{q_u^2}{2})^{\frac{1}{2}}, \quad (3.13)$$

Thus the parameters a , q , and β are related to the characteristic frequencies making up the ion trajectory. For low values of β (i.e. $\beta=0$ to $\simeq 0.4$), the amplitudes of high-frequency oscillating terms in the ion trajectory are small compared with those at fundamental frequency [28]. In this case, we can neglect the high-frequency oscillating terms, so the ion trajectory for low β can be described as

$$u(t) \approx A \cos \omega_{u,0} t + B \sin \omega_{u,0} t \quad (3.14)$$

This satisfies the equation

$$\frac{d^2 u}{dt^2} + \omega_{u,0}^2 u = 0 \quad (3.15)$$

We can see this equation actually describes a simple harmonic oscillation along the u -axis. This means we can consider that these ions are following a simple harmonic motion when β is low. Examples of calculated ion trajectories are given in Figure 4.1.

3.2 Pseudopotential Well of the Trap

For a single ion trapped in a Paul trap, the β oscillation can be thought of as an oscillation in a pseudopotential well Φ_{ps} , which comes from both the static potential

from the dc voltage and the average effect of the RF voltage. In fact the pseudopotential well doesn't exist until an ion is actually held in a stable trajectory within the trap.

We may calculate the pseudopotential Φ_{ps} [30, 31]. For a trap operating with both dc and RF voltages, the potential $\Phi_{ps}(x, y, z)$ at a point $x, y,$ and z is

$$\Phi_{ps}(x, y, z) = \frac{m}{2e} \left(\frac{\Omega}{2}\right)^2 \left(a_r + \frac{q_r^2}{2}\right) (x^2 + y^2) \quad (3.16)$$

$$\begin{aligned} &+ \frac{m}{2e} \left(\frac{\Omega}{2}\right)^2 (-2a_r + 2qr^2) z^2 + constant \\ &= D_r \frac{r^2}{r_0^2} + D_z \frac{z^2}{z_0^2} + constant \end{aligned} \quad (3.17)$$

D_r and D_z represent the pseudopotential well depth in the radial and axial directions respectively and their equations are:

$$D_r = \frac{mr_0^2}{2e} \left(\frac{\Omega}{2}\right)^2 \left(a_r + \frac{q_r^2}{2}\right) \quad (3.18)$$

$$D_z = \frac{mz_0^2}{2e} \left(\frac{\Omega}{2}\right)^2 (-2a_r + 2qr^2) \quad (3.19)$$

The pseudopotential well depth concept is useful. One can visualize the trapped ions motion like the motion of particles in a real potential well. In section 3.4, we looked a correlation between pseudopotential well depth and trapping efficiency as reflected in number of ions trapped.

3.3 Experimental procedure of trapping stability and efficiency tests

In the study of trapping stability, the trap is operated with an (a, q) value which lies within the stable area ($0 < \beta_{r,z} < 1$) of the stability diagram (Figure 3.2) so the ions can be confined inside the trap with stable trajectories. As we discussed in

section 3.1, the (a,q) value is determined by the physical operating parameters of the ion trap. For our present system, $r_0 = 20.3\text{mm}$, and the trapped ion is ^{232}Th : i.e. $m=232$ amu. The adjustable parameters are RF voltage, frequency and DC voltage. By varying these parameters, a and q values change so the trap can be operated at different positions on the stability diagram.

Besides stability, efficiency is also important. The stable (a,q) values need to be searched to find the best trapping conditions to trap many ions. A series of experiments were done to test our present ion trap and find the best operating conditions by varying the adjustable operating parameters: RF frequency and voltage.

Before the trapping experiments, factors which may affect the creation of the ions, such as laser desorption intensity and timing, and the wavelength and energy of the resonant ionization are optimized. In general, ions are accumulated in the trap by repeating the desorption and RIS laser pulses ten times to minimize laser shot to shot variation in producing and trapping of the desired ions. A hydrogen buffer gas pressure of 10^{-3} Pa is used to cool the ions produced, and the ions are stored for about 10 seconds before they are extracted. The measured TOF spectrum is monitored by a MCP detector. Through the area under the mass peak of TOF spectrum which corresponds the ^{232}Th , the number of Th ions trapped is determined. The number of ions trapped and stored at different RF frequencies and voltages is an important indication of trap operating conditions. Through these measurements, the trapping efficiency, stability and working range of our trap system can be determined and the best operating parameters can be deduced.

3.4 Ions trapped as a function of RF voltage at fixed frequency

The first experiment we did was to measure the number of ions trapped at different RF voltages while the frequency was kept at a constant value and no dc bias was

applied. Figure 3.3 shows a typical result obtained at $f=150$ kHz.

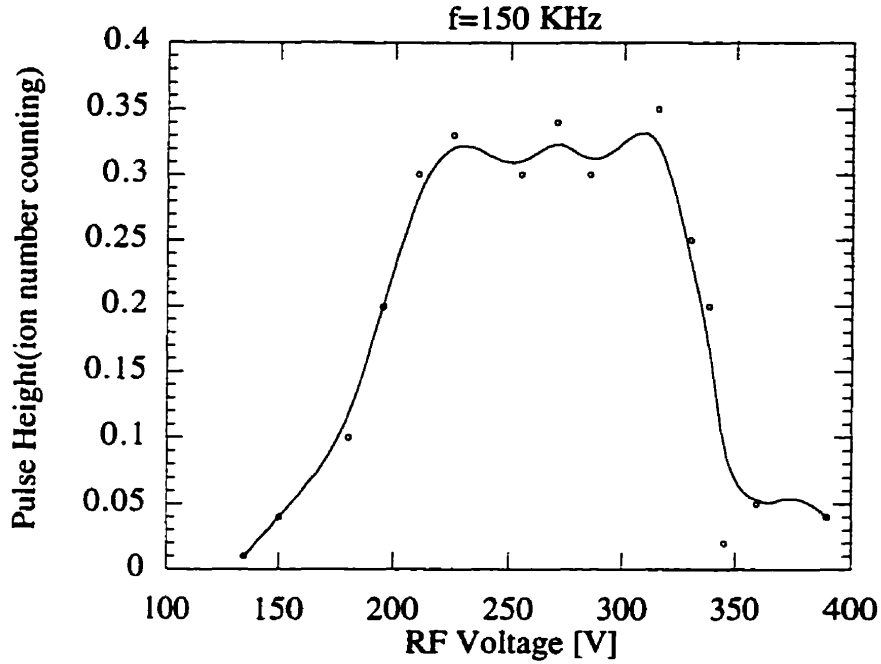


Figure 3.3: Ion number vs RF voltage at $f=150$ kHz

The voltage range covered is from 135V to 390V which corresponds to q_z values from 0.30 to 0.88. The results show that there is a low voltage threshold (V_{low}) below which very few ions are being trapped. Above this point the number of ions trapped increases dramatically. There is also an upper voltage threshold (V_{high}) above which the number of trapped ions drop suddenly. These lower and upper voltage thresholds correspond to q_z values of 0.43 and 0.79 respectively. The a-q stability diagram in Figure 3.2 suggests that one can expect stable ion orbits between $q_z=0$ and $q_z=0.90$ with $a_z=0$. Our results indicate that the practical range of q_z is smaller than this. This is probably due to the imperfect shape holes in the electrodes and mechanical

f_{rf} (kHz)	V_{low} (V)	$q_{z,low}$	V_{high} (V)	$q_{z,high}$
150	190	0.43	350	0.79
160	200	0.40	370	0.73
170	200	0.35	400	0.70
180	260	0.41		
190	280	0.39		
200	310	0.39		
210	290	0.33		
220	330	0.35		
230	330	0.32		

Table 3.1: Results Table

alignment.

Similar experiments were done at RF frequencies from 150 kHz to 230 kHz in 10 kHz steps. For each RF frequency, we recorded a plot similar to Figure 3.4. The RF voltage ranges are recorded and shown in table 3.1. For $f > 180$ kHz, we didn't obtain a high voltage cutoff point for each frequency, because the operating voltage lies outside the limit of the RF amplifier.

The results of table 3.1 show that for each frequency, the $q_{z,low}$ values and the $q_{z,high}$ values change little. It reveals that as long as we keep the operating condition within the stated q_z region, the trapping is stable and efficient.

The pseudopotential well-depth values of the low threshold points at different frequencies in table 3.1 are calculated and listed in table 3.2. The calculation results reveal that those low cutoff points have roughly the same well-depth value. This suggests that a minimum well depth potential is necessary to efficiently trap ions at any RF frequency.

At $f = 180$ kHz, we have also examined the effect of the DC voltage from 0V to 25V

f_{rf} (kHz)	$q_{z,low}$	D_z (eV)
150	0.43	2.5
160	0.40	2.5
170	0.35	2.2
180	0.41	3.3
190	0.39	3.4
200	0.39	3.8
210	0.33	3.1
220	0.35	3.5
230	0.32	3.3

Table 3.2: D_z values for low cutoff points

while q_z was kept at a constant value. Increasing the DC voltage means that the value of a in the stability diagram (Figure 3.2) moves lower toward a higher β direction. The results show that varying a value does affect the low cutoff voltage point. The best trapping trend moves toward higher DC voltage, but the total maximum ion number trapped remains the same.

3.5 Trapping efficiency vs f_{RF} with constant q_z

With a constant q value, the trapping efficiency at different frequency (f_{RF}) and amplitude was also investigated. Figure 3.4 is a plot of ion numbers vs operating frequency at $q_z = 0.40$. It indicates that at each frequency, the number of ions trapped is relatively constant. There is a slightly better trapping (more total ions) toward higher frequency.

The result can be explained if related to the trap pseudopotential well-depth. At the same q value, the well depths at lower frequencies are shallower than the well

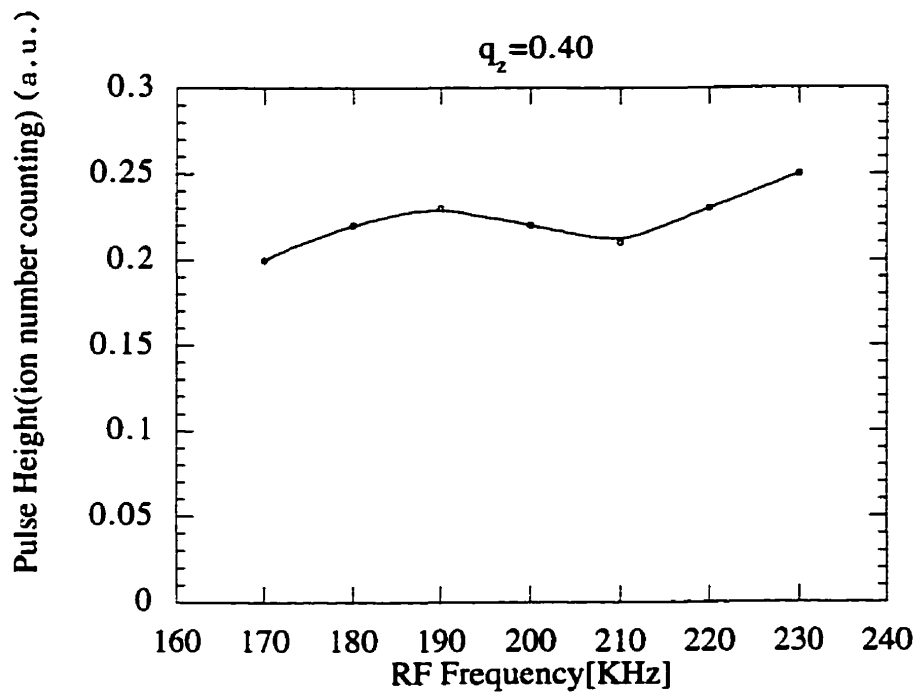


Figure 3.4: Ion number vs operating frequency at $q_z=0.40$

depths at higher frequencies.

3.6 The storage time of trapped ions and chemical reaction inside trap

Trapping efficiency also includes how long the trap can confine the ions inside the trap. The storage time of trapped ions is very important for laser spectroscopy.

An ion trapped will remain inside the trap unless its trajectory is disturbed. There are several factors which affect the motion of ions inside the trap. Among them, the two main factors are collisions and chemical reactions.

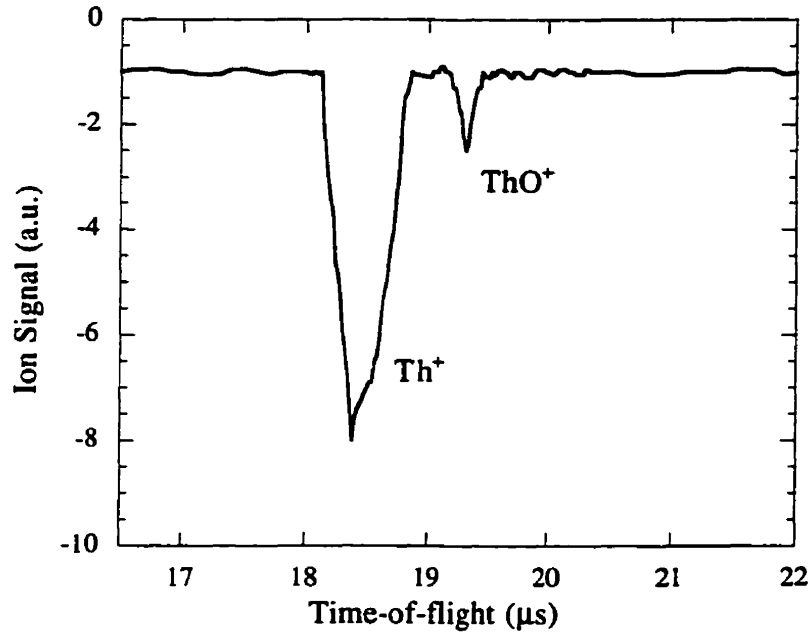
An ion's collision with other particles can scatter it to a different trajectory. Collisions with the light atoms of a buffer gas usually take energy away and cause an ion to condense towards the center of the trap. But if the buffer gas pressure is too

high, the confinement is destroyed and the ions will diffuse from the trap. Collisions with heavy particles, and particularly coulomb collisions with other ions, are likely to scatter the ions out of the trap.

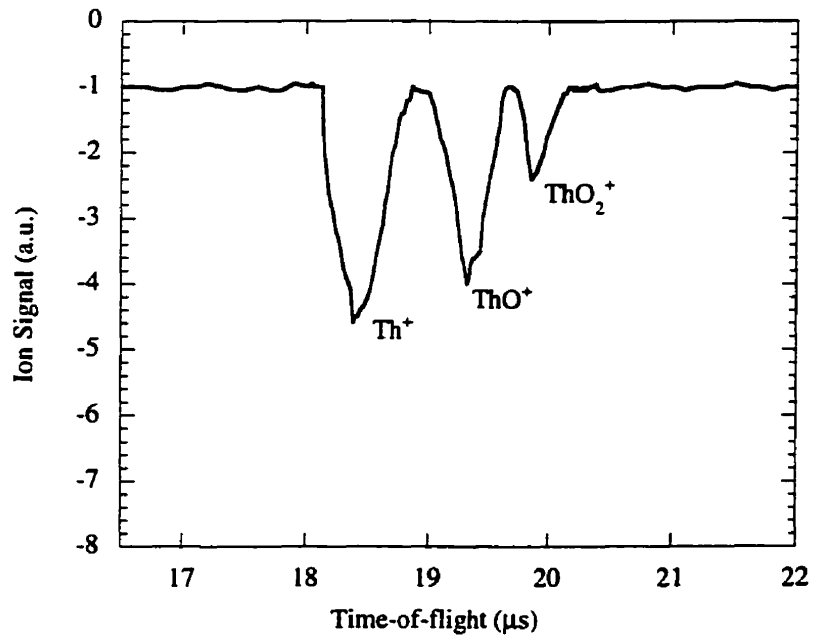
Not all the ions confined inside the trap can be detected with laser-induced fluorescence. Ions which have chemically combined with contaminants in the trap have a changed electronic energy level structure, so the ions are no longer excited by the original ion resonant laser wavelength. There is also a problem of metastable states. Some atomic/ionic electron systems have low-lying states from which transitions to the ground state are forbidden. If an excitation scheme has decay channels to the metastable states, then continued excitation from the ground state will populate those metastable states and deplete the ground state. Metastable states can't decay by spontaneous fluorescence but can be quenched by collision with buffer gas molecules.

In our experiments, Hydrogen buffer gas was used for quenching the Th ions to the ground state and cooling the ions to keep them in the center of the trap. Experiment results showed that without buffer gas, the trap couldn't hold many ions, and most of the ions escaped from the trap. The storage time of Th was only a hundred seconds. With buffer gas, the storage time of Th increased to about 10 minutes and the maximum number of ions accumulated was about 5000.

Figure 3.5 shows typical time-of-flight spectra of trapped Th and Th oxide ions. We obtained these spectra after storing ions for 30 seconds and 5 minutes respectively. We can see the conversion of two different masses. The first TOF spectrum shows only two different masses which are Th^+ and ThO^+ . After ions were stored 5 minutes, the TOF spectrum shows three different mass peaks. The shifts in TOF of the extracted peaks suggest the peaks result from a chemical conversion from Th^+ to ThO^+ and from ThO^+ to ThO_2^+ ions.



(a)



(b)

Figure 3.5: TOF measurement shows the Th and Th oxide conversion. (a): Ions extracted after storing inside the trap about 30 seconds (b): Ions extracted after stored inside the trap about 5 minutes

There are two possible sources of the oxygen with which the thorium combines. There is oxygen which comes from outgassing of the chamber and trap elements and there is some residual oxygen in the hydrogen buffer gas. In order to reduce the outgassing we baked the system and ran the titanium sublimation pump as described in section 2.5. As for the buffer gas, we tried to find the lowest pressure which would give good capture and retention of the ions in the trap while introducing as little contaminant oxygen as possible. The storage time can be improved to 10 minutes or longer, which enable us to measure linewidths and relative trapping and confinement efficiencies.

3.7 Conclusion

We have found that for our trapping system, over a quite wide range of RF frequency and voltage, ions can be trapped stably and efficiently. Adding a DC voltage on the ring electrode moves the operating point towards higher β , and extends the lower cutoff RF voltage value. We also found that Th can react easily with oxygen inside the trap to form ThO^+ and ThO_2^+ . After storing Th ions inside the trap for 10 minutes, around 50 percent of ions converted into ThO^+ and ThO_2^+ . Comparing with storage time of approximately one hour for Hf experiments in this lab, the storage time of Th^+ inside the trap is not as long as we expected.

Chapter 4

Trapped Ion Motion and Phase Space Dynamics

When ions interact with incident laser beam in a Paul trap, the resonances in their absorption spectra are broadened due to the motion of the ions under the influence of the confining rf field. The non-relativistic Doppler shift $\Delta\nu$ due to the motion of an ion is given by

$$\Delta\nu/\nu_0 \propto v/c \quad (4.1)$$

Where v is the mean velocity of the ions and c is the velocity of light. Under normal operating conditions, the trapped ions may have an average kinetic energy of 0.2 eV. This will correspond to a Doppler broadening of 2.1 GHz with a typical wavelength of 322.8 nm.

One way to reduce this Doppler broadening effect is to limit the observation of the LIF photon to a particular phase of the applied RF field. This can be accomplished by using phase-locked detection.

In this chapter, the basic principles of trapped particle dynamics and phase space are presented, and a possible approach for reducing Doppler broadening are discussed. The experimental methods and results are described and discussed, and the minimum

temperature of the ion cloud is deduced.

4.1 Particle Dynamics and Ion trajectories as a function of time

Classical physics tells us that if we know the initial position and velocity of a particle and the forces acting on it, we can calculate its future position and velocity. In cases like that of a particle in a parabolic potential well $f = -kx$, it is possible to solve the equation of motion and find equations which describe the particle's position and velocity as a function of time.

From $F = -kx$, we have

$$m \frac{d^2 x}{dt^2} = -kx \quad (4.2)$$

If we assume x has the form $Ce^{\omega t}$ then

$$Cm \frac{d^2 e^{\omega t}}{dt^2} = -Cke^{\omega t} \quad (4.3)$$

which gives

$$\omega^2 = -\frac{k}{m} \quad (4.4)$$

or

$$\omega = \pm i \left(\frac{k}{m} \right)^{\frac{1}{2}} \quad (4.5)$$

This tells us that

$$x = x_0 \cos \left(\left(\frac{k}{m} \right)^{\frac{1}{2}} t \right) \quad (4.6)$$

where x_0 is the value of x at $t=0$.

For ions trapped inside a Paul trap, the equation of motion is a form of the Mathieu equation described in chapter 3. This equation does not have simple closed solutions. However, we can numerically integrate the ion equations of motion presented in section 3.1 and plot out ion trajectories as a function of time.

In order to plot the trajectories in physical and phase space, we use a 4th order Runge-Kutta routine and integrate the equation of single ion motion (3.3)(3.4) derived directly from a 1-dimensional quadrupole electric field as presented below:

Start with E being a restoring field linear with x :

$$E(x) = -2kx \quad (4.7)$$

Since the field is the negative gradient of the potential,

$$\phi = -\int E(x)dx = kx^2 + C \quad (4.8)$$

In 3 dimensions,

$$\phi = k_1x^2 + k_2y^2 + k_3z^2 + C \quad (4.9)$$

If $\nabla^2\phi = 0$, then $k_1 + k_2 + k_3 = 0$; We choose $k_1 = k_2 = -k_3/2$, then

$$\phi = kx^2 + ky^2 - 2kz^2 + C \quad (4.10)$$

as

$$\phi_{r=r_0} = V_0 \cos \omega t + U_0, z = 0 \quad (4.11)$$

and

$$\phi = 0, x = y = 0, z = r_0/\sqrt{2} \quad (4.12)$$

at $x = r_0$ and $y = z = 0$

$$V_0 \cos \omega t + U_0 = kr_0^2 + C \quad (4.13)$$

at $z = r_0/\sqrt{2}$ and $x = y = 0$

$$0 = -kr_0^2 + C \quad (4.14)$$

so

$$C = kr_0^2 \quad (4.15)$$

$$k = \frac{V_0 \cos \omega t + U_0}{2r_0^2} \quad (4.16)$$

$$E_r = -\frac{r(V_0 \cos \omega t + U_0)}{r_0^2} \quad (4.17)$$

$$E_z = \frac{2z(V_0 \cos \omega t + U_0)}{r_0^2} \quad (4.18)$$

the equation of motion is

$$F = \frac{md^2x}{dt^2} \quad (4.19)$$

which leads to

$$\frac{d^2r}{dt^2} = -er \frac{V_0 \cos \omega t + U_0}{mr_0^2} \quad (4.20)$$

and

$$\frac{d^2z}{dt^2} = 2ez \frac{V_0 \cos \omega t + U_0}{mr_0^2} \quad (4.21)$$

which are the ion equations of motion presented as equations(3.3)(3.4) in Chapter 3. In the simulation, the initial velocity of the ion is assumed to be zero. An RF cycle is divided into 100 points. This determines the size of the time step taken.

Figure 4.1a shows the trajectory of a particle in a static parabolic potential well. Figures 4.1b and 4.1c present the ion trajectories for different values of rf voltage and frequency and d.c. bias. The particle in the parabolic well executes simple harmonic motion and the trajectory is sinusoidal. We plotted the ion motion along the r-axis since in our experimental work we are probing ions along the r-direction. At $\beta_r=0.15$, the ion trajectory is similar to that of the particle undergoing simple harmonic motion shown in Figure 4.1a, but some ripples are superimposed on the simple harmonic motion. At $\beta_r=0.85$, although there is still some periodic structure,

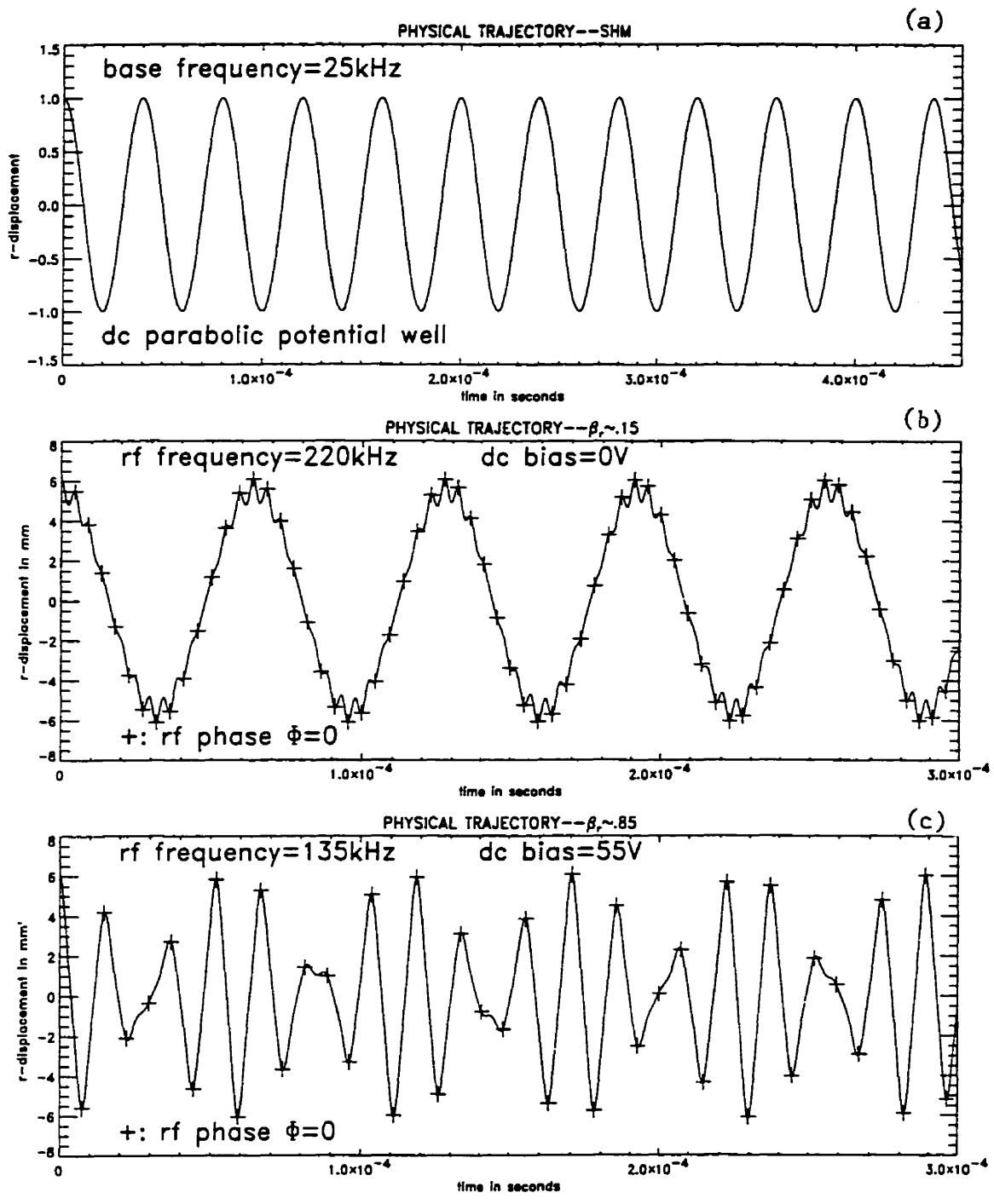


Figure 4.1: Trapped ion trajectories

the trajectory is significantly distorted compared to the trajectory at $\beta_r=0.15$. The ion motion seems irregular at the high β_r value.

To relate these single-particle trajectories to the phase-locked detection which reduces the Doppler broadening, it is helpful to consider the two-dimensional action diagrams which are projections of the 6-dimensional phase space volume occupied by the trapped ions. In order to understand the action diagrams, we need to first understand what is phase-space and what we mean by phase-space volume here.

4.2 Phase space and phase trajectories for trapped ions

Phase space is a six-dimensional space defined by combining the ordinary 3-dimensional spatial space and the 3-dimensional momentum space together. A particle can be represented as a point in phase space by position and momentum coordinates at any particular time.

If the motion of a particle in three orthogonal directions x, y , and z can be considered independently of one another (i.e. the motions in the three coordinates are decoupled), the phase space can be separated into three phase planes, (x, x') , (y, y') , and (z, z') where $x'=dx/dt$, $y'=dy/dt$, and $z'=dz/dt$. Those phase-planes are called two-dimensional phase-space action diagrams plotting momentum vs displacement [28, 29].

For particles in a quadrupole field, the force is proportional to the displacement from the origin. The motion that results from application of a steady force is simple harmonic. The trajectory of a particle undergoing simple harmonic motion in a phase plane is an ellipse centered on the origin and with its axes aligned with the momentum and displacement axes. Figure 4.2a shows such a simple phase space trajectory. The phase space volume specifies the volume occupied by the phase trajectory.

In a Paul trap, if the effect of the RF micro-motion is neglected, the ion oscillates

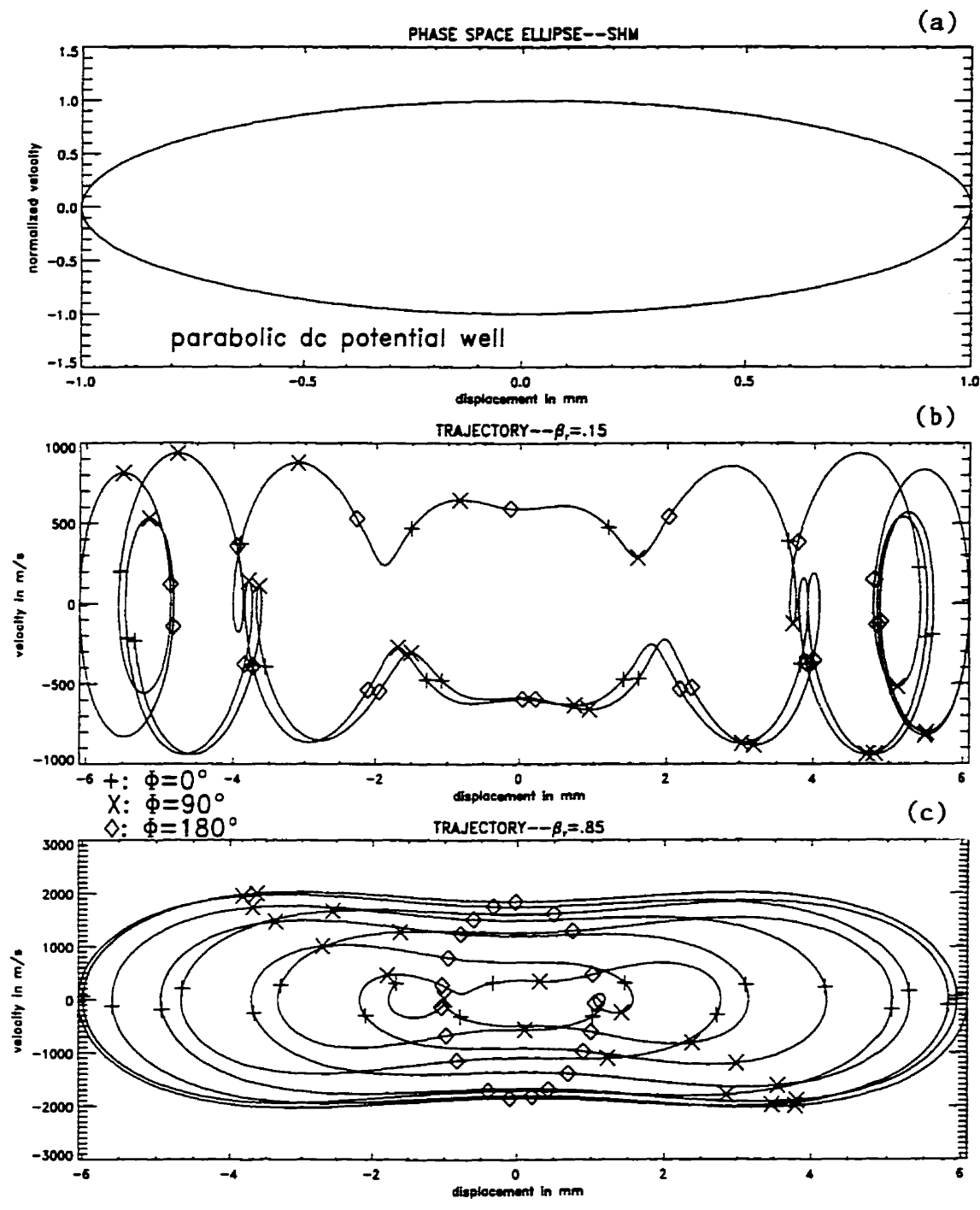


Figure 4.2: Ion trajectories in phase space-I

with simple harmonic motion which is a simple phase space trajectory just like the trajectory shown in Figure 4.2a. But, when the RF frequency micro-motion is included, the simple elliptical phase space diagram is distorted [32]. From a numerical integration calculation, the phase trajectories for ions inside the trap are plotted for two different β_r values in Figure 4.2b and 4.2c.

At first glance, the phase trajectories shown in figures 4.2b and 4.2c, reveal no simple structure. However if we only look at points at specific rf phase intervals, indicated with different symbols for different phase angles in figures 4.2b and 4.2c, elliptical patterns begin to emerge. In figures 4.2b and 4.2c we see that the single particle trajectory crosses a particular ellipse at various points at a given rf phase angle but that at that given rf phase angle it will always be found on the corresponding ellipse. These ellipses are drawn without the interposing trajectory points in figure 4.3a and 4.3b.

4.3 Variation of phase space ellipses with different rf phase angle and trap operating parameters

Figure 4.3 plots out the simulation results of the family of phase space ellipses for ion motion in the r direction at the operating points $\beta_r=0.15$ and $\beta_r=0.85$ demonstrating the variation of shapes and orientation of the ellipse with the change of the RF phase. In figure 4.3, the x-axis stands for distance from the trap center in the r direction and the y-axis is the velocity in the r direction. It can be seen that under different β_r values the extension of the phase diagram along the vertical axis, which indicates the velocity spread of an ion cloud in the radial direction, changes with the RF phase. In general, at each plot, at 0° RF phase, the ion motion along the radial direction reaches a minimum. This suggests that laser spectroscopic measurements gated at 0° phase can be used to improve the spectral resolution.

We further see that the shape of the ellipses not only varies according to the rf

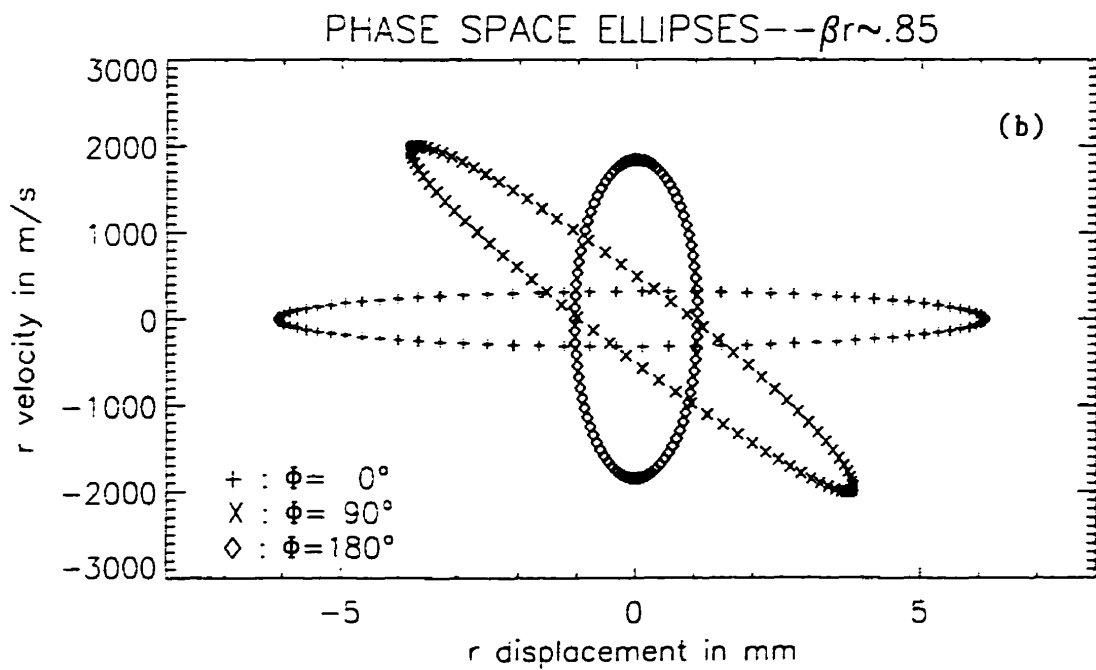
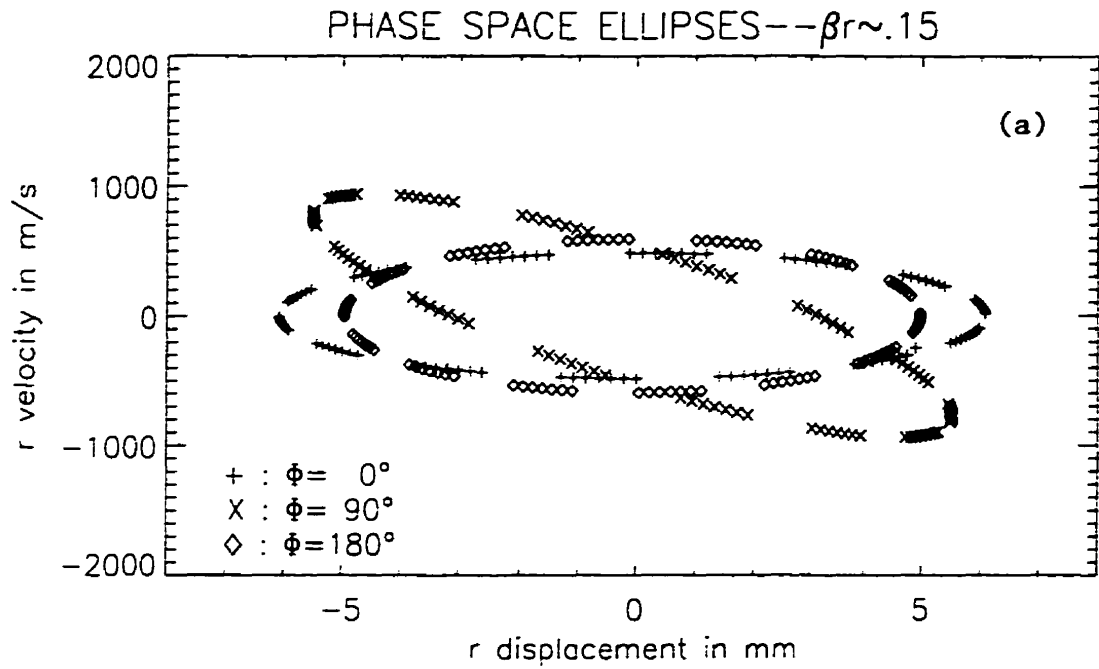


Figure 4.3: Ion trajectories in phase space-II

phase angle but also varies for different trap operating parameters. Choosing a very low β value and a very high β value within the trapping stable range discussed in Chapter 3, the trap phase-space ellipses at $0^\circ, 90^\circ$ and 180° at $\beta_r=0.15$, and $\beta_r=0.85$ are quite different.

At $\beta_r=0.15$, the shape of the trap phase-space at different RF phases ($0^\circ, 90^\circ, 180^\circ$) remains similar. The extension of the 0° phase-space ellipse along the velocity axis in the radial direction shows a smaller velocity spread compared to the 90° and 180° phase ellipses. Between the 0° and 180° ellipses, there is little difference in the velocity spread.

At $\beta_r=0.85$, the shape of the ellipses are distorted dramatically, and the extension of the distorted ellipses along the velocity axis varies with RF phase. The 0° phase-space ellipse still exhibits the minimum velocity spread, but the shape of the ellipse is elongated, and the velocity spread is reduced compared to the ellipse of 0° at $\beta_r=0.15$. For the 180° phase-space ellipse, the velocity spread increases about 4 times compared to the spread of 0° phase.

If we look at the ellipse corresponding to 0° rf phase in the family of ellipses generated from the trajectory calculated from $\beta_r=0.85$ (Figure 4.3b) we see that no ions within 6mm of the center of the trap will have velocities greater than 300m/s at times near the crest of the rf signal. Returning to figure 4.1c we see that these points are points at which the rf field is causing the particle to change direction and so its radial velocity is nearly zero. The difference between the velocity spread on different rf phase ellipses is not nearly as great for the family of ellipses corresponding to $\beta_r=0.15$, although it is clear that the minimum velocity spread corresponds to rf phase=0. It follows that observation around this point in time will yield the minimum Doppler broadening and that it should be possible to get the smallest line width by operating the trap with parameters such that β_r is large.

4.4 $\Delta\nu$ Versus RF Phase Angle Measurement

Through the above phase space calculation, we know that the velocity spread of the ion cloud and also their Doppler linewidth $\Delta\nu$ vary with the RF phase. This variation of the spectral linewidth can be measured by phase-selective LIF de-excitation.

To start the measurement, after the ions are loaded, the tunable cw laser beam is modulated to excite the ions at a particular RF phase during a time period which is about 300 ns (much shorter than the RF cycle period). Meanwhile, the de-exciting fluorescence photons from those ions are recorded by RF phase-locked coincidence counting.

In the study, sample ^{232}Th was used. At a given RF phase, the LIF spectrum was obtained by scanning the probing uv laser wavelength across the resonance frequency which is 322.8 nm. Since the even-even Th isotope gives a single resonance peak and the laser linewidth is negligible, the spectral linewidth corresponds to the velocity spread of the ion cloud in the trap. Figure 4.4 records the narrowest ^{232}Th lines we measured at operating point $a=0$, $q_z=0.495$ with a gate width of 170ns covering about 20 degrees of rf cycle centered around 0° phase. Operating under these conditions we observed fluorescence resonance which fit well with a Gaussian of the full width at half maximum (FWHM) of 720 MHz.

The spectral linewidths at different phases were also measured. The result is shown in Figure 4.5. From the spectra presented we can see the change of the linewidth with the RF phase. The FWHM data showing linewidth variations at different phases is compiled and demonstrated in Figure 4.6a. These experimental width variations can be compared to the theoretical calculation results from the phase-space diagrams shown in Figure 4.6b. In general, the experimental results shown in Figure 4.6a agree well with the calculation from phase-space dynamics. The experiments qualitatively reproduce the 0° phase minimum linewidth result and the slight variation of $\Delta\nu$ at 0° and 180° phase. These results follow the trend

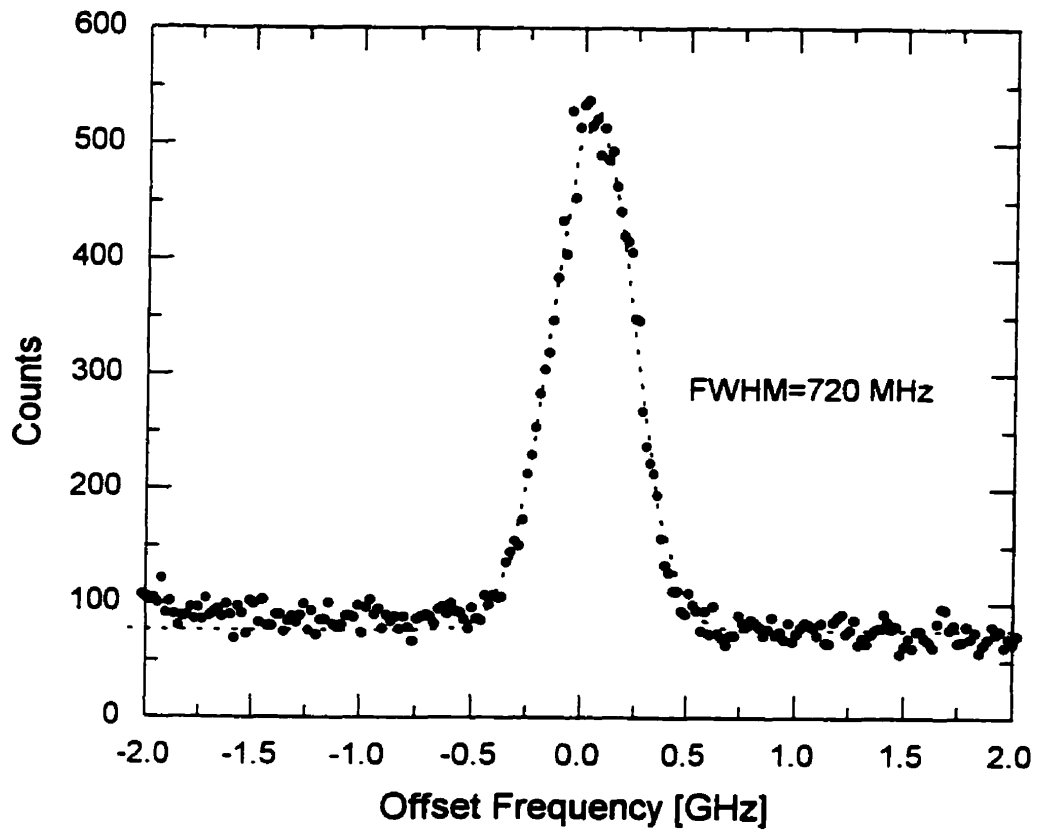


Figure 4.4: The Th spectrum pumped at 322.8 nm

suggested by the calculation curve. However, the experimental data at 90° and 270° rf phase region showed much larger velocity spread than that of the simulation. This is probably because we didn't consider the interaction of ions with each other in our calculation. At 90° and 270° rf phase region, the ions inside the trap have higher velocity and therefore more interaction between ions would occur.

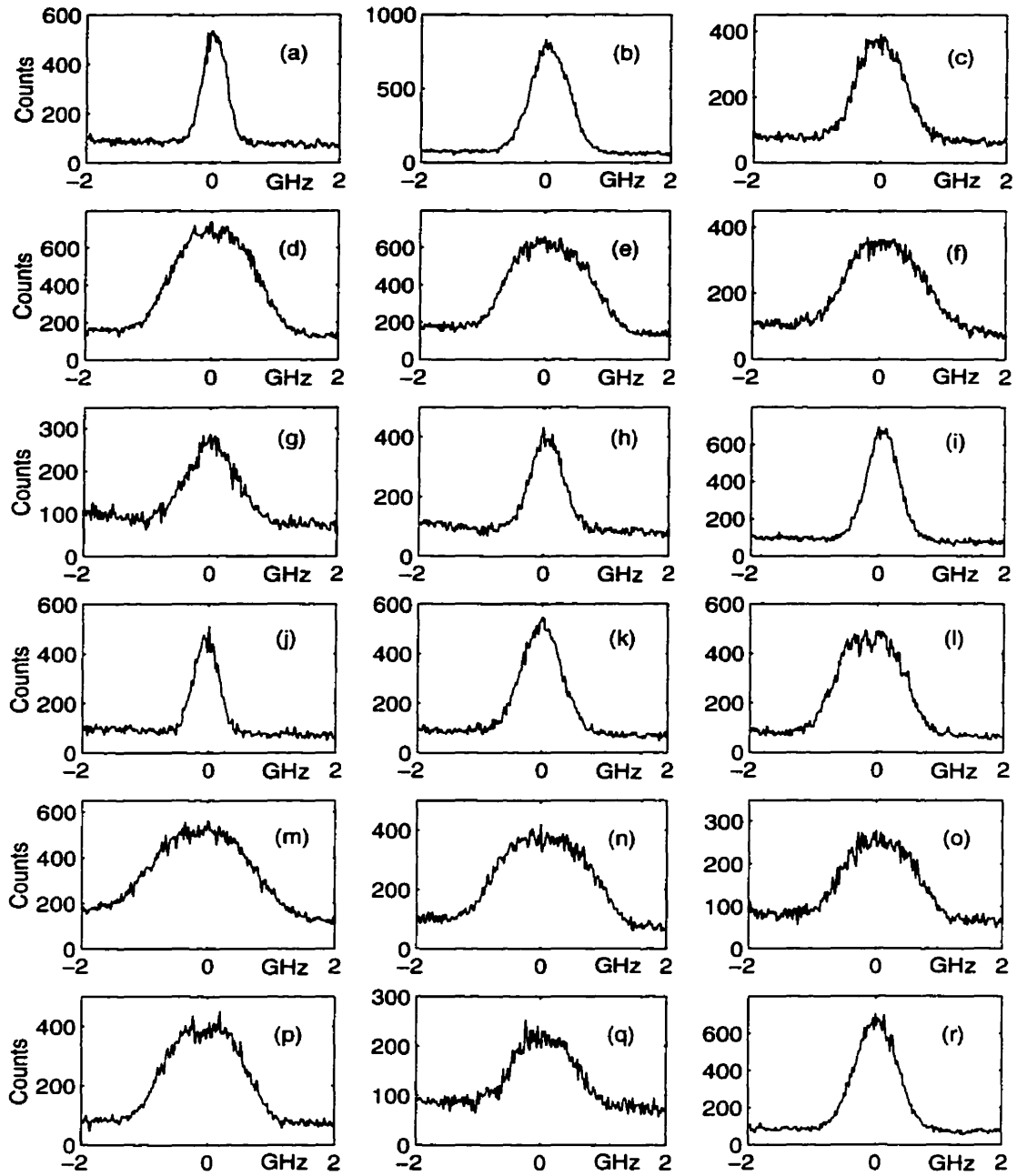


Figure 4.5: A group of laser spectra at different RF phase angles measured by phase-selective LIF. The Trapping condition is $a_z = 0$, $q_z = 0.495$. (a) to (r) correspond the RF phase angle from 0° to 340° where each has 20° difference. The variation of the spectrum linewidth is due to the variation of the velocity spread of the ions along the radial direction.

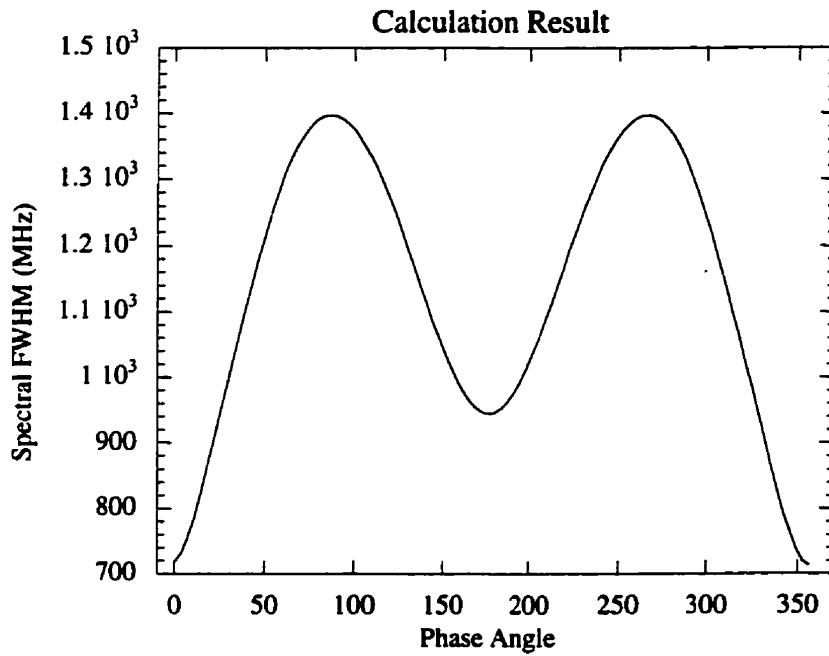
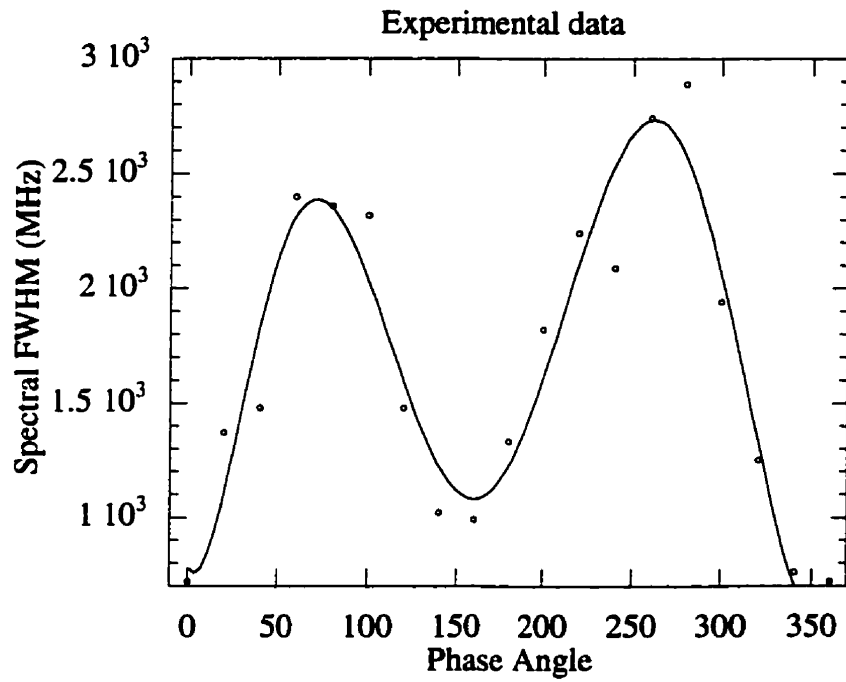


Figure 4.6: Spectral full width(FWHM) vs RF phase angles. The data correspond to operating condition ($a_z=0$, $q_z=0.495$)

4.5 $\Delta\nu$ Versus RF phase angle at different β_r value

From the simulation, one can expect that if we go to higher β_r , at 0° phase the linewidth should decrease and 180° phase it should increase. It is tempting to try to run experiments at higher β_r .

From our normal operating point, we reached a lower β_r and a higher β_r . The linewidths of the spectra were then measured by phase-selective coincidence counting at 0° and 180° phases at low $\beta_r=0.15$ and $\beta_r = 0.35$ respectively. At $\beta_r=0.15$, at 0° , the linewidth is 770 MHz, at 180° , The linewidth is 870 MHz. There is about 100 MHz difference between these two phases. At $\beta_r=0.35$, the linewidth at 0 phase is 720 MHz, while the line width at 180° phase is 1 GHz. There is about 300 MHz difference.

From this result, we can see that indeed at 0° the linewidth decreased when the β_r value varied from 0.15 to 0.35, and at 180° it increased. However, for our trap system, at higher β_r , the number of ions trapped inside the trap is fewer. Running at higher β_r does improve the spectral resolution, but it decreases the efficiency of the trapping. We were unable to operate the trap at higher rf voltages, so we were unable to operate trap at much higher β_r . Further research is needed to explore the situation at higher β_r .

However, thermodynamic considerations suggest that it is unlikely we could gain much even if we could move to a higher β_r regime.

4.6 Ion Temperature

Our numerical integrations show the trajectories of single ions under the influence of the rf quadrupole fields. The action diagrams show that the possible positions and velocities of particles at particular phase points in the rf cycle fall on ellipses. At high β_r and 0° rf phase the spread of possible velocities for ions with a given maximum displacement from the center of the trap can be very small (Figure4.3b).

If the ions did not interact, it would be reasonable to assume that many ions could be packed into the trap at various points along the action ellipse or inside it, and that a measurement of the velocity spread by Doppler broadening of a narrow resonance line would show a narrow line.

However, both the buffer gas and the coulomb interaction of the ions with each other would tend to perturb the trajectories calculated for non-interacting particles. It is important to distinguish random thermal motion from the more or less coherent motion of the ions under the influence of the trapping fields. Random thermal motion should prevent the trapped ions from exhibiting a linewidth narrower than that of a population of ions with a Maxwell-Boltzmann velocity distribution and a specific temperature. Because the ions are cooled by interaction with a buffer gas, it is generally accepted that ions in the trap are in thermal equilibrium with the buffer gas.

When a particle velocity distribution reaches a thermal equilibrium, it can be described by a Gaussian for any one of the canonical coordinates [33].

$$dN(v_x) = N \sqrt{\frac{m}{2\pi kT}} \exp\left(-\frac{m}{2kT} v_x^2\right) dv_x \quad (4.22)$$

with

$$\sigma(v_x) = \sqrt{\frac{kT}{m}} \quad (4.23)$$

where kT is the average thermal energy with ion temperature T and The full width at half maximum of such a velocity distribution is [34]

$$\frac{\Delta\nu}{\nu} = 2\sqrt{\ln 2} \frac{v}{c} \quad (4.24)$$

where v is the mean velocity of ions. As we measured a linewidth of 720 MHz by LIF measurement at 0° phase, with $\lambda=322.8$ nm, the minimum temperature of trapped ions deduced from equation (4.23) and (4.24) is $T=330$ K and $kT=0.028$ eV. This ion temperature is very close to room temperature. It is unlikely that we would be able

to improve much on this result by going to a higher β_r . Compared with Wenzheng's previous Hf result of $T=450\text{K}$ [18], the Th ion temperature is sounded low. This is due to the different RF driving frequency used. Wenzheng's normal operating RF frequency was at 400 kHz while ours was at 200 kHz. According to Wenzheng [18], with the RF driving frequency 250 kHz, he measured a 900 MHz linewidth of ^{178}Hf which corresponds to a kT less than 0.031 eV. This is consistent with our result.

4.7 Conclusion

We reduced the Doppler broadening of the spectral lines of trapped ions by counting photons for a period of time which is short compared to the length of an rf cycle and synchronize the gate with the rf phase. This process is better understood by relating the ion motion with phase space volume occupied by the trapped ions. Both calculation and experimental results show that the velocity spread of the ion cloud and their Doppler linewidth vary with the RF phase and the best linewidth(720 MHz) is achieved with phase-selective detection at 0° phase. The minimum ion temperature correspond to this linewidth is 330 K. Operating the trap at different β_r value affects the Doppler linewidth. The simulation results showed a trend to run the trap at relatively high β_r , however, for our present system, running the trap at higher β_r sacrificed the efficiency of the trapping. In addition, the ion temperature calculation suggested that we wouldn't reduce much more on linewidth even if we could run at a higher β_r .

Chapter 5

Optimizing Detection of LIF from Th Ions

Since our main goal is to evaluate the feasibility of studying ^{229}Th in our present system and the radioactive ^{229}Th source is only available in ng to pg amounts, the experiment requires a high sensitivity. In addition to maximizing production, capture and storage of Th ions, we also need to optimize excitation and detection.

Detection sensitivity is determined by several factors. Among these are the type of optical detector used, the excitation scheme employed, and the optical alignment. We observed several transitions of ThII using ^{232}Th with two different photomultipliers. In this chapter, after an introductory description of the properties of Th and a short review of previous Th work, the Th ion production process is described. Five different ThII excitation schemes are examined, and the experimental results are compared with regard to signal to background ratio and spectral sensitivity.

5.1 Thorium: Nuclear Properties and Previous Isotope Research Review

Thorium is a silvery-white metal and belongs to the actinide series of elements. Its electronic configuration is $[\text{Rn}] 7s^2 6d^2$. It has an ionization potential of 6.95eV and the melting point is 2023.2K. Thorium is a radioactive element. ^{232}Th has the longest half-life (1.4×10^{10} y) among *Th* isotopes.

Thorium is in the Ra-Th region ($220 < A < 230$) in which experimental results show an unusual feature in the structure of nuclei [35, 36, 37]. A common feature observed in the usual isotopic variation of the mean-square charge radii is the so-called odd-even staggering: the radius of an odd-N isotope is slightly smaller than the average radius for two even-N neighbors. However, for the nuclei between $A = 220$ and 226 (Fr, Ra, etc), experiments show an inversion of the normal odd-even staggering. Theorists ascribe this feature to an intrinsic octupole deformation of the nucleus [38, 39, 40].

Since the thorium isotopes lie in this mass region, they are of considerable interest. In the past, measurements of the optical isotope shift and the hyperfine splitting for a few thorium isotopes have been performed using discharge lamps and Fourier transform spectrometers or grating spectrographs [41, 42, 43] [44] [45, 46]. With these methods, the isotope shifts between ^{230}Th and ^{232}Th [41, 42, 43] and between ^{229}Th and ^{232}Th [44], as well as the hyperfine splittings for ^{229}Th have been determined for several optical transitions [45, 46]. From the analysis of the ^{230}Th - ^{232}Th isotope shift data, the change of the mean square charge radius between these two isotopes has been evaluated [47, 48].

More detailed and extended information on unstable Th isotopes has been obtained by using high-resolution and highly sensitive laser spectroscopic methods. In 1988, Th isotopes were measured first by laser spectroscopy on stored ions in a Paul trap by a group from Germany [16]. In order to fill Th ions into the trap, they coated some dry Th nitrate solution on a tantalum wire which was mounted inside the trap,

and heated the wire to a high temperature (about 2000K). The evaporated material was then ionized by an electron beam. The stored Th ions were optically excited by light from tunable cw lasers; two different excitation schemes were applied in their experiments [16, 17]. With single step excitation, the ThII transition ($\lambda=583.9$ nm) from the ground state to the state at 17122 cm^{-1} is induced. The excitation was observed by detection of the fluorescence of the spontaneous transition into the metastable state at 1522 cm^{-1} . From this scheme, the FWHM value achieved was 1 to 1.6 GHz. For the two step excitation method, two overlapping and counter propagating laser beams excited the subsequent transitions ThII $0 \rightarrow 17122\text{ cm}^{-1}$ at $\lambda=583.9$ nm and $17122\text{ cm}^{-1} \rightarrow 34544\text{ cm}^{-1}$ at $\lambda=573.8$ nm. The combined excitation was monitored by detection of the fluorescence of the transitions at $\lambda=332.6$ nm, 358.9 nm, and 367.3 nm, leading into the states around 6000 cm^{-1} . With the two step excitation, the resolution obtained was about 350MHz, and the sensitivity of the method is improved compared with the sensitivity of one step excitation, and sample sizes of only 10 pg were required for the experiment [17].

From the above experiments, isotope shifts and hyperfine splittings in optical transitions for atomic ions of the Th isotopes ^{227}Th to ^{230}Th and ^{232}Th were measured. The hyperfine splitting for ^{229}Th for 3 electronic levels was also determined. From the Th isotope shift data, changes of the mean square charge radii were determined. The German group therefore concluded that for Th nuclei the transition to an inverted staggering and the possible onset of octupole deformation do not occur in the same way as for Fr and Ra [16].

In addition, as discussed in the introduction, Th is particularly interesting to us because it has been predicted that there exists a first excited state of isotope ^{229}Th , with $J^\pi = 3/2^+$ within 3.5 ± 1.0 eV of the $5/2^+$ ground state [22]. With the splitting of only a few eV, it becomes very attractive for study of the resonance interaction between the nucleus and the electronic shell.

This low energy metastable level of ^{229}Th can be populated by α decay of ^{233}U .

Careful measurement of the energies of subsequent γ rays resulted in this excitation energy [21]. However, The existence of this metastable level has not yet been directly observed in any experiment. With an excitation energy below that of the most loosely bound atomic electron in thorium, the decay of the excited state may not be able to proceed via internal conversion process, but it might excite transitions between bound atomic levels. It is challenging to excite the electron cloud of Th using direct laser excitation. If we can trap the recoil ^{229}Th from ^{233}U α decay in the Paul trap. we can measure the optical hyperfine structures of the low energy isomer and the ground state, thus confirming the existence of such as isomer.

5.2 Th Ion Production Process

In order to fill the trap with thorium ions, a Nd:YAG laser beam($1.06\mu\text{m}$) is used to evaporate neutral ^{232}Th atoms from the target substrate. then the desorbed atoms can be resonantly ionized and trapped. Generally the laser desorption process depends on the laser intensity and the target surface conditions. We want the desorbed material to be in the neutral atomic form, so the YAG beam size and intensity are carefully adjusted to avoid the production of contaminant ions and to maximize the yield of neutral Th atoms.

The desorption laser intensity can be adjusted by changing the laser pulse energy, laser repetition rate and its focusing condition. In general, a repetition rate of 2-6 Hz was used. Laser pulse energy was about 1 mJ per pulse. A lens with focal length of 30cm placed outside the vacuum chamber produced a well focused laser spot with a diameter of 1-1.5 mm for desorption.

After the neutral atoms are produced by the YAG beam. We use laser resonant ionization to selectively ionize the neutral atoms of Th into Th ions. In Resonance Ionization Spectroscopy(RIS), atoms of a specific element are brought up by one or a series of resonant transitions to a high-lying excited state from which they can be

ionized by further excitation to a level beyond the the ionization limit. The excitation between the discrete states is easily saturated because of the high excitation cross-sections, typically around 10^{-14} cm^2 . But the final ionization step is usually from a discrete state to continuum transition, which has a much smaller cross-section. A high laser pulse energy for the final step is usually needed to enhance the ionization efficiency [49].

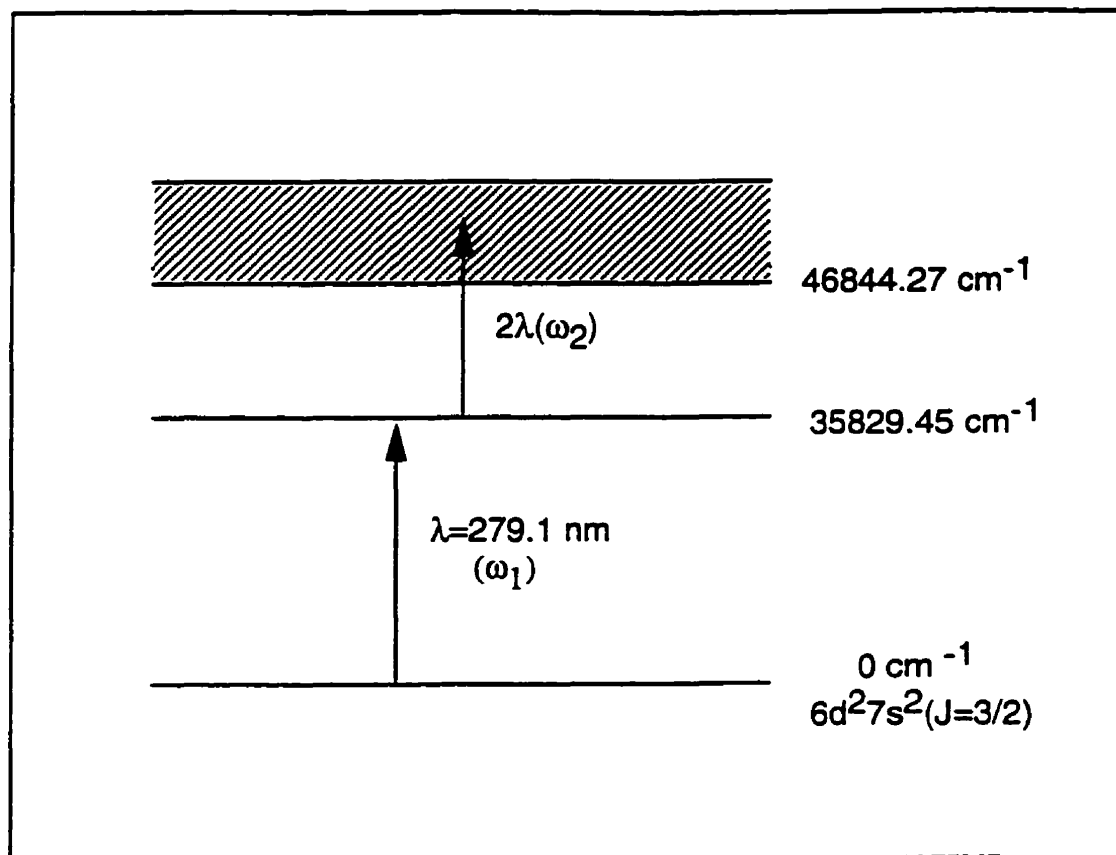


Figure 5.1: The RIS scheme of Th

The RIS scheme of Th that we used is shown in Figure 5.1. To produce Th ions through the RIS process, a pulsed dye laser (with dye C540A) pumped by an excimer laser is used. A uv laser pulse with wavelength 279.1 nm after frequency doubling is for the first excitation step from $E=0 \text{ cm}^{-1}$ to $E=35829.45 \text{ cm}^{-1}$. The green fundamental beam of about 10mJ to 20mJ per pulse is used for the second ionization step. The ionization level of ThII has been determined as 46844.27 cm^{-1}

by double-resonance, field ionization spectroscopy.

From Chapter 4, we know that an ion produced in the trap will remain inside the trap if the ion is produced with a position and velocity that fall on a stable phase space trajectory. From the discussion in Chapter 3, it is known that collisions and chemical reactions are the main factors which affect the storage time of ions.

In the present case, with proper buffer gas cooling, our LIF measurements can only be conducted for about 15 minutes before most of the *Th* ions are converted into *ThO*⁺ ions. Therefore, after a series of repeated scans was completed, fresh ions were reloaded again for the next series of scan. This procedure means that data obtained with different samples can cause some fluctuations in the deduced results.

5.3 Laser Spectroscopy Measurements

5.3.1 LIF Detection Procedure

After the ²³²*Th* ions have been loaded into the trap, the stored *Th* ions are optically excited by light from tunable cw dye lasers. This is accomplished by sending the probing cw beam through the holes on the ring electrode of the trap and hitting the ion clouds. The LIF is detected by monitoring the spontaneous emission following the induced excitation. In these experiments, the photomultiplier detects not only the fluorescence photons from de-exciting but also photons from the incident cw light and other visible background. A common problem we faced in the experiments is how to reduce the background counts and improve the signal-to-background ratio of the photon-counting detection. The background counts are mainly from two sources: Photomultiplier dark current and scattered photons from the probing beam. The photomultiplier dark current is mainly due to thermionic emission [34]. To minimize the dark current counts, the signal pulses pass through a pulse height discriminator. The discriminator threshold level is carefully adjusted to suppress the dark current

without affecting the fluorescence count rate.

Once the dark current counts are minimized, the main source of background is from pump laser photons which reach the detector. Scattered light from the laser beam is then reduced by carefully aiming the laser, collimating the incident beam, and using apertures and lenses and a light dump after the beam passes through the chamber. In addition, proper filters are placed in front of the photomultiplier to discriminate against scattered laser light and other background luminescence.

To detect the resonance, the probing beam wavelength is scanned over the resonance while the PM output rate is recorded on the computer. Each scan takes about 1 minute and usually 10 scans are taken at each measurement. The modulator for the laser beam and the phase-locked coincidence requirement were then added, and fine tuned to optimize the single-to-background ratio of the resonance.

In the present work, we have carried out the measurements for five excitation transition in Th^+ . These are tabulated in Table 5.1.

Table 5.1: Thorium Lines Detected and Detection Results

No	λ_{laser} in nm	Production method	$I_{excitation}$	λ_{decay} in nm	I_{decay}	PM used	Energy Levels in cm^{-1}	Filters used	Background Counts(cps)	S/B ratio (Maximum)
1	343.6	A	770	362.6	390	1	29095.5-1521.9	WG360+UG5	1500	12
2	327	A	110	348.3	130	1	30564.57-1859.94	WG345+UG5	350	8
3	322.8	A	110	372.2 372.6 *343.4	340 220 980	1	30972.16-4113.36 30972.16-4146.6 30972.16-1860	WG360,WG345,UG5	300	25
4	291.2	B	90	355.9 365.8	530 420	1	34330.5-6244 34330.5-7001	WG345	300	10
5	583.9	C	10	640.86 *768.6	19 21	1,2	17121.6-1521.9 17121.6-4113.36	F640,RG610,RG630	20	65

A: Inter-cavity Frequency Doubling method B: External Frequency Doubling method C: Fundamental laser method

1: RCA 8850 Photomultiplier 2: RCA 31034 Photomultiplier

*: Lines we were unable to observe, but found in the compiled ThII transition tables

5.3.2 Experimental Results

Table 5.1 summarizes the experimental results. In the table, line 1 represents the case where the wavelength of the pumped laser (λ_{laser}) is 343.6 nm, representing the transition from the ground state to the state 29095.5 cm^{-1} . The laser beam is produced by using intercavity frequency doubling method (indicated as method A in column 3 of the table). The de-excitation was observed by the detection of the fluorescence of the spontaneous transition to the metastable state at 1521.9 cm^{-1} (shown in Energy levels column of the table). This subsequent de-excitation transition corresponds to the decay wavelength of 362.6 nm (λ_{decay}). Judging from the relative intensities of these transitions ($I_{excitation}$ and I_{decay}), about 30 percent of the decay proceed photons with the emission of 362.2 nm. Filters WG360 and UG5 are used to reject the scattered pump laser and background light. The detection is accomplished using the photomultiplier RCA 8850 (shown as PM 1 in column 7). For this transition, although we measured high signal counts (18,000 cps), the high background encountered resulted in a signal-to-background ratio (S/N ratio in the table) of 12 only. This is probably because the WG360 filter is not sufficient to reject the primary laser scattered light.

For the excitation transition of 327 nm (line2), the same laser production method and detection photomultiplier were used. The excitation was monitored by detection of the fluorescence of the transition at $\lambda=348.3 \text{ nm}$ which corresponded to the initial and final energy levels of 30564.57 cm^{-1} and 1859.94 cm^{-1} respectively. Filter WG345 and UG5 were used to block the scattered laser and background light. The background counts we measured was 350 cps and the best signal-to-background ratio obtained was 8. The background counts are much less than that of line 1 but the signal counts are even lower, only 2800 cps.

For line 3, $\lambda_{laser}=322.8 \text{ nm}$, two de-excitation channels were observed at $\lambda=372.2 \text{ nm}$ and $\lambda=372.6 \text{ nm}$. We obtained 300 background counts and a good signal-to-background ratio of 25 representing a peak signal of 7500 cps. Filters WG345 and

WG360 were more suitable to detect this line than line 1 and 2. In addition, the doubling crystal operating range and the DCM dye range are also more favorable for the production of this laser beam.

For line 4 at 291.2 nm, we used an external crystal to double the probing wavelength. Using filter WG 345, we were able to suppress the primary laser at $\lambda=291.2$ nm sufficiently and transmit as much as possible the subsequent fluorescence at $\lambda=355.9$ nm and $\lambda= 365.8$ nm. The intensities of this de-excitation transition indicates almost 90 percent of the decay proceed photons. This would represent a very favorable line for the detection of the Th ions. However, We measured 300 cps background counts and only obtained a signal-to-background ratio of 10. Although the background counts rate is acceptable, the resulting S/N ratio is still low. This is mainly due to the low UV intensity after the doubling crystal, and it was difficult to control the probing laser power and stability.

Working with the visible line pumped at 583.9nm had the advantage that there was no doubling crystal involved so laser alignment was easier and the available power of the fundamental laser was much greater. We measured this line twice, once with an RCA8850 photomultiplier and once with an RCA31034 photomultiplier. The quantum efficiency of the RCA8850 falls rapidly for longer wavelengths; at 640nm, it is only 1 percent. The quantum efficiency of the RCA31034 remains high up to the near IR and is about 18 percent at 640nm. Along with filters RG610 and RG630, we used filter F640 to detect this visible line. This F640 filter has a high transmission rate (73 percent) at 641 nm and a narrow width of 10 nm. The background counts from scattered light were further suppressed by the combination of these filters. We measured a very low background counts, 20cps and a good signal-to-background ratio of 65. However, the absolute signal counting rate of 1300 cps is somewhat low.

Considering all the results and factors above, two lines are favorable to us. One is the UV line pumped at 322.8nm. The other is the visible line pumped at 583.9nm.

5.3.3 Discussion

From these compiled data, for the de-excitation to 372.2 and 372.6 nm pumped at 322.8 nm (line3), the background count rate is 300 cps and the signal count rate is 7500 cps. From the TOF signal this spectrum represents 2000 ions inside the trap. We measure 3.75 fluorescence counts per ion per second. So a signal-to-background ratio of 1:1 could be obtained with 80 ions trapped inside the trap.

For the decay detected at 640.86nm which is pumped at 583.9 nm (line 5), background counts are low, only about 20 cps. With the signal-to-background ratio of 65, the signal counts are 1300 cps. Considering about 3500 Th ions contributed to this spectrum, we measured 0.37 fluorescence counts per ion per second. This means if we want to have a signal-to-background ratio of 1:1, 60 ions are required. The extremely low fluorescence counts per ion per second of this line means that in the experiments longer counting time is needed to overcome this problem, so in a practical sense, if we can only store the ions inside the trap for a few minutes, the spectral sensitivity will be very limited by statistical fluctuation of the data obtained.

According to Wenzheng's Hf work in this lab, he deduced that 10 ions of isotope ^{178}Hf yielded a signal-to-background ratio of 1:1. Compared with 6 fluorescence counts per ion per second he measured, using the same photomultiplier, in UV range, for line pumped at 322.8 nm, we measured about 4 fluorescence counts per ion per second and the background counts are 4 times higher. This is due to the filtering and alignment. We need to search better filters to further suppress the background of line 3. Furthermore, for the line 5, with the cooled photomultiplier RCA 31034, we only measured 0.37 fluorescence counts per ion per second. Judging from the detection quantum efficiency of different photomultipliers used at the observed wavelengths, we should be able to measure 2-3 fluorescence counts per ion per second for line 5. One of the reasons for the low counts rate is that the quantum efficiency of the detection of line 5 is low. We have many filters in the way which cut down the background but also cut down the overall efficiency of the detection. In addition, because this cooled

photomultiplier has a narrower detection window, it is possible that the collection beam is not well focused onto the photocathode. We can further improve the focusing condition of the lens in front of the photocathode of the photomultiplier so that we can have a higher photon collection efficiency and increase the counts rate of line 5.

The above ions signal-to-background ratios are based on the measurements of ^{232}Th . ^{232}Th is an even isotope and has nuclear spin $I=0$ so that the levels are unsplit and no hyperfine structure is present. For this isotope, we therefore observe a single spectral line. If we observe even-odd isotopes, there is hyperfine structure distribution. The spectral lines will spread out and the strength of each spectral line will be less, therefore, more ions are required in the experiment.

Along with the narrow linewidth (720 MHz) achieved by phase-selective LIF at zero phase, the overall spectral sensitivity of our LIF measurements indicates that trapping more than a hundred ^{229}Th ions would be sufficient to carry out the proposed ^{229}Th experiment. Furthermore, the overall sensitivity can be improved by increasing the Th storage time. A thorough clean-up of the trap assembly would be necessary before the ^{229}Th source is put inside the trap, and baking the chamber afterwards at higher temperature would also make some progress on storage time.

Considering the proposed ^{229}Th experiments, one approach is to use ^{229}Th source extracted from ^{233}U . We can use our ion injection system and put the ^{229}Th into the trap. After baking the trap chamber, the ^{229}Th can be desorbed and ionized by the laser pulses. If the low energy isomer is still there, through LIF detection, we should see the hyperfine structure which is different from that of the ^{229}Th ground state. However, such a process is very long. It can take a couple of days preparation before we carry out the experiment. If the lifetime of the low energy isomer is shorter than that, we can not detect the isomer in this way. It would be much better if we can get the recoil ^{229}Th from ^{233}U direct α decay. We can do the experiments in a shorter time through recoil method. The available ^{233}U source is a continuous decay source and can produce thousands of fresh ^{229}Th atoms every second. If we can put

the ^{229}Th ions produced inside the trap, we should be able to carry out the proposed experiments. However, since the ^{229}Th atoms obtained from α decay have a energy of 70 KeV, and the trap has a very limited size demension, it is hard to slow ions down and confine them inside the trap. The next challenge in our lab is to find an efficient way to transport the ions into the trap.

Chapter 6

Summary and Conclusion

In this work, a series of experiments were done to explore the possibility of studying ^{229}Th in our present system. The sample we used is pure metallic ^{232}Th , which is placed near the inner surface of the ring electrode of our Paul trap system. The production of Th ions is accomplished by using the desorption laser (Nd:YAG laser) beam and the synchronized RIS pulse laser beam. The Th ions trapped in a Paul trap can be confined inside the trap for a period of time, while the ions can be extracted out and their mass spectrum and the number of ions determined by time-of-flight detection, or the tunable cw laser beam can be used to probe ions. And LIF is monitored for spectroscopic measurements.

First, the stability of the trapped ions and the trapping efficiency have been investigated under various operating conditions for our Paul trap. Through TOF measurement, the RF frequency and voltage were varied over a wide range to see their effects on the number of trapped ion inside the trap. It has been found that at each RF frequency, there is an operating region of voltage amplitude which corresponds to a region in the stability diagram in which we can obtain stable and efficient trapping condition. We found no advantages to operating at any specific frequency which were not related to our equipment limitations.

Further studies have been done on evaluation of the effects of various trap op-

erating parameters and RF phase on spectral resolution. By gating the window of observation and synchronizing the gate with the RF phase, the Doppler broadening due to the ion motion is reduced and spectra with a 720 MHz resolution in UV range were obtained. The understanding of this process is improved by studying the phase space trajectories of ions inside the trap. Both simulations and experiments were done to study the variation of the resolution (corresponding to velocity spread of ion motion) produced by changing the RF phase. The results showed that the ion motion along the r direction reaches its minimum at zero RF phase. Studies also show that by increasing β_r , we can further improve the spectral resolution at 0 phase. However, thermodynamics considerations suggest that there is a limit to the improvements that can be realized.

Moreover, a detailed study has been carried out in order to evaluate the sensitivity and the resolution of different optical excitation and detection schemes. Through studying five different ThII transitions in the UV and visible ranges, two lines have been selected as favorable candidates for the proposed ^{229}Th detection. One is the UV line pumped at 322.8 nm and the other is the visible line pumped at 583.9 nm. It is concluded that 60-80 trapped ions can yield a 1:1 signal-to-background ratio spectrum from these two detection schemes. There is reason to believe the sensitivity of the cooled photomultiplier can be further improved by alignment.

In conclusion, this thesis covers three aspects of feasibility studies of detecting ^{229}Th by laser spectroscopy in our Paul trap system. Our results give us confidence to undertake the proposed experiments on ^{229}Th in future work.

Bibliography

- [1] E.W.Otten. In D.A.Bromley, editor. *Treatise on Heavy Ions Science Vol.8: Nuclear Far From Stability*, volume Ch7. Plenum press. New York. 1989.
- [2] J.E.Crawford. in Proc. of Int.Conf. on Nucl.Shapes and Nucl.Struct. at Low Excitation Energies, Antibes, France, 1994.
- [3] J.Billowes and P.Campbell. *Phys.G: Nucl.Part.Phys.*, 21:707. 1995.
- [4] Pierre Jacquinet and Robert Klapisch. Hyperfine spectroscopy of radioactive atoms. *Rep.Prog. Phys.*, 42:773–832, 1979.
- [5] E.G.Nadjakov and K.P.Marinova. *At.data and nucl.data tables*. 56:133. 1994.
- [6] S.L.Kaufman. *Opt.Commun.*, 17:309, 1976.
- [7] W.A.Wing, G.A.Ruff, W.E.Lamb, and J.J.Spezeski. *Phys.Rev.Lett.*, 36:1488. 1976.
- [8] Ernst Wilhelm Otten. Laser techniques in nuclear physics. *Nuclear Physics*. A354:471–496, 1981.
- [9] G.D.Alkhazov, A.E.Barzakh, V.P.Denisov, V.S.Ivanov, I.Ya.Chubukov, V.N.Fedoseev, V.S.Letokhov, V.I.Mishin, and S.K.Sekatsky. *Hyperfine Interaction*, 61:1335, 1990.

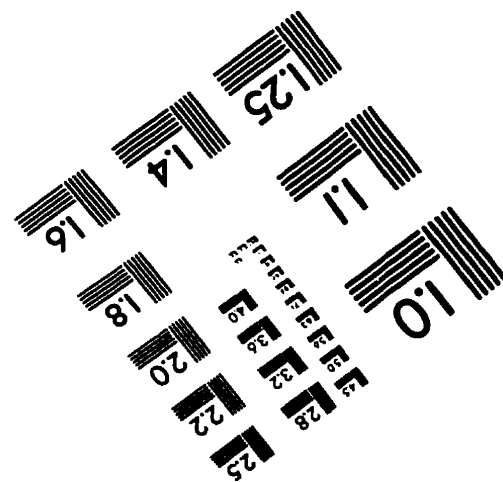
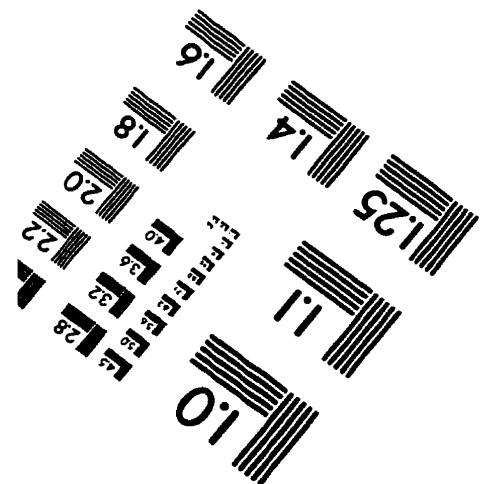
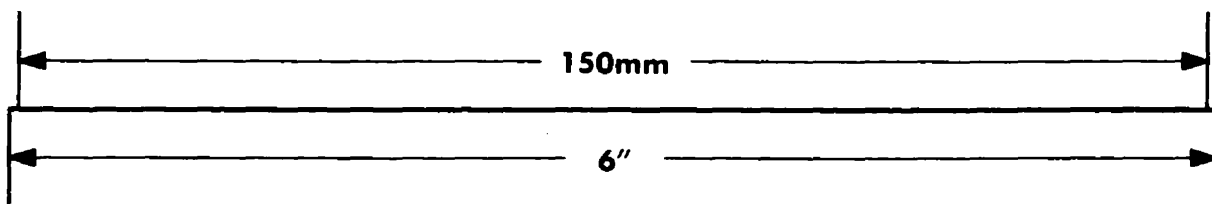
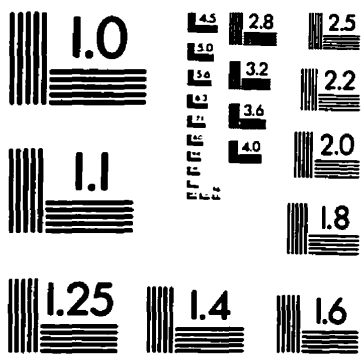
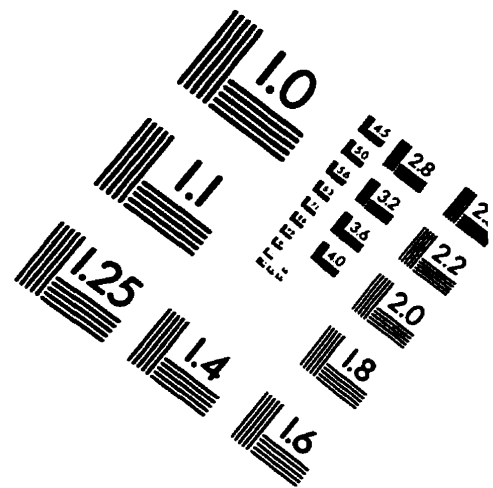
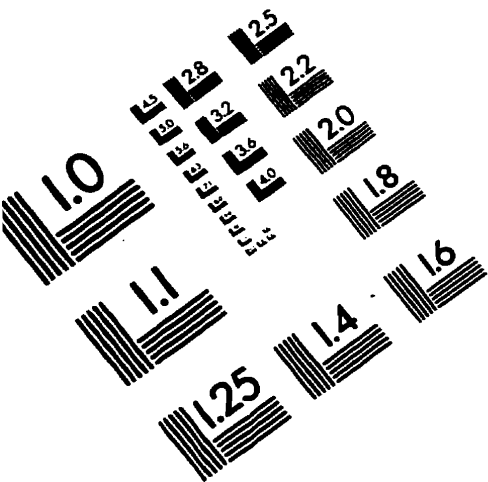
- [10] J.K.P.Lee, J.E.Crawford, Z.Raut, G.Savard, G.Thekkadath, H.T.Duong, and J.Pinard. *Nucl.Instrum.Methods Phys.Res.*, B(26):444, 1987.
- [11] U.Krönert, St.Becher, Th.Hilberath, H.-J.Kluge, and C.Schulz. *Applied Physics*, A(44):339, 1987.
- [12] W.Paul, O.Osberghaus, and E.Fischer Forschungsber.Wirtsch. Verkehrsministeriums Nordrhein-Westfalen. No.415(1958);. *E.Fischer,Z.Physik*, 156:1, 1959.
- [13] W.Neuhauser, M.Hohenstatt, P.E.Toschek, and H.Dehmelt. *Physics Review*, A22:1137, 1980.
- [14] R.Ifflander and G.Werth. *Metrologia*, 13:167, 1977.
- [15] J.Rink, B.Gorski, W.Kälber, G.Meisel, H.J.Mielke, H.Rebel, and M.Schubert. *Z.Phys.*, A(342):487, 1992.
- [16] W.Kälber, J.Rink, K.Bekk, W.Faubel, S.Göring, G.Meisel, H.Rebel, and R.C. Thompson. Nuclear radii of thorium isotopes from laser spectroscopy of stored ions. *Z.Phys.A-Atomic Nuclei*, 334:103–108, 1989.
- [17] W.Kälber, G.Meisel, and J.Rink. Two-step optical excitation for doppler linewidth reduction and motion study of ions stored in a paul trap. *Modern Optics*, 39(2):335–347, 1992.
- [18] WhenZheng Zhao. Laser spectroscopic studies of hafnium ions confined in a paul trap. PhD thesis,McGill University, 1995.
- [19] W.Z.Zhao, F.Buchinger, J.E.Crawford, S.Fedrico, S.Gulick, J.K.P.Lee, O.Constantinescu, M.Hussonnois, and J.Pinard. *Hyperfine Interactions*, 20, 1996.
- [20] W.Z.Zhao, F.Buchinger, J.E.Crawford, S.Gulick, J.K.P.Lee, O.Constantinescu, M.Hussonnois, and J.Pinard. *Spectrochimica Acta, Part B*, 51:707–712, 1996.

- [21] C.W.Reich and R.G.Helmer. Energy separation of the doublet of intrinsic states at the ground state of ^{229}Th . *Physics Review Letters*, 64(3):271–273, Jan. 1990.
- [22] R.G.Helmer and C.W.Reich. An excited state of ^{229}Th at 3.5 ev. *Physical Review C*, 49(4):1845–1857, April 1994.
- [23] F.F.Karpeshin, I.M.Band, M.B.Trzhaskovskaya, and B.A.Zon. *Phys.Lett.*, B(282):267, 1992.
- [24] J. Wycech, S.;Zylicz. *Conference Paper at International Symposium on Nuclear Physics of our Times*, 1992.
- [25] F.F.Karpeshin, I.M.Band, and M.B.Trzhaskowskaya. Neet revisited in connection with the resonance radiative pumping of ^{229}Th . *American Institute of Physics*, pages 468–471, 1995.
- [26] M.D.N.Lunney, F.Buchinger, and R.B.Moore. *Modern Optics*, 39:349, 1992.
- [27] J.F.O’Hanlon. A user’s guide to vacuum technology, 2nd edition, 1989.
- [28] In Peter H.Dawson, editor, *Quadrupole Mass Spectrometry and its applications*. Elsevier Scientific Publishing Company, 1976.
- [29] Rolf Engleman Jr.and Byron A.Palmer. *Opt.Soc.Am.B*, 1(6):782–787, December 1984.
- [30] R.D.Knight and M.H.Prior. *Applied Physics*, (50):3044, 1979.
- [31] S.Guan and A.G.Marshall. *Am.Soc.Mass Spectrom.*, 5:64, 1994.
- [32] R.B.Moore and M.D.Lunney. The paul trap as a collection device. CRC Press, March 1994.

- [33] R.B.Moore and M.D.N.Lunney. Ion trap instruments. In R.E.March and J.F.J.Todd, editors, *Practical Aspects of Ion Trap Mass Spectrometry*, volume II. CRC Press, Boca Raton, 1995.
- [34] Wolfgang Demtröder. In *Laser Spectroscopy, Second Edition*. Springer, 1996.
- [35] Schüler P. and Lauterbach Ch. and Agarwal Y.K. and etc. *Physics Letter*, B(174):241, 1986.
- [36] Ward D., Dracoulis G.D., Leigh J.R., Charity R.J., Hinde D.J., and Newton J.O. *Nuclear Physics*, A(406):591, 1983.
- [37] Bonin W., Backe H., Dahlinger M., Glienke S., Habs D., Hanelt E., Kankeleit E., and Schwartz B. *Z.Phys.A- Atoms and Nuclei*, (322):59, 1985.
- [38] Leander.G.A., Sheline, R.K., Möller.P., Olanders.P., Ragnarsson .I, and Sierk A.J. *Nuclear Physics*, A(388):452, 1982.
- [39] Nazarewicz W, Olanders, et al. *Nuclear Physics*, A(429):269, 1984.
- [40] Robledo, L.M., Egido, J.L., J.F., and Girod.M. *Phys.Lett.*, 187(B):223, 1987.
- [41] Stukenbroeker G.L. and Mc.Nally and Jr.J.R. *Opt.Soc.Am.*, 43:36, 1953.
- [42] Engleman Jr.R. and Palmer B.A. *Opt.Soc.Am*, 73:694, 1983.
- [43] Engleman Jr.R. and Palmer B.A. *Opt.Soc.Am*, B(1):782, 1984.
- [44] Vernyi E.A. and Egorov V.N. *Opt.Spectrosc.*, 9:367, 1960.
- [45] Egorov V.N. *Opt.Spectrosc*, 16:301, 1964.
- [46] Gerstenkorn S., P. Luc, Verges J. and Englekemeir D.W., Gindler J.E., and Tomkins F.S. *J.Phys.(Paris)*, 35:483, 1974.
- [47] Blaise J. and Steudel A. *Z.Phys.*, (209):311, 1968.

- [48] Aufmuth P., Heilig K., and Steudel A. *At.Data Nucl.Data Tables*, (37):455, 1987.
- [49] G.S.Hurst and M.G.Payne. In *Principles and Applications of Resonance Ionization Spectroscopy*. Adam Hilger and Bristol and Philadelphia, 1988.

IMAGE EVALUATION TEST TARGET (QA-3)



APPLIED IMAGE, Inc
 1653 East Main Street
 Rochester, NY 14609 USA
 Phone: 716/482-0300
 Fax: 716/288-5989

© 1993, Applied image, inc., All Rights Reserved